



Characterization Tools for Mechanical Probing of Biomimetic Materials

2

Silvia Caponi, Claudio Canale, Ornella Cavalleri, and Massimo Vassalli

Contents

1	Overview	69
2	Introduction	70
3	Experimental and Instrumental Methodology	71
3.1	Scanning Probe Microscopy	72
3.2	Brillouin Spectroscopy	80
4	Key Research Findings	89
4.1	Indentation Experiments on Hard/Soft Materials	90
4.2	Mechanical Properties of Porous Materials for Tissue Engineering	93
4.3	Noncontact Mechanical Analysis	95
5	Conclusions and Future Perspective	104
	References	105

1 Overview

The possibility to fully heal damaged or failing tissues and organs is one of the major challenges of modern medicine. Several approaches have been proposed, either using tissue engineered functional substitutes or inducing the body to self-repair, exploiting its innate regenerative potential. In any case, a crucial step for the success of therapy is provided by the design of a suitable scaffold, capable to sustain cellular growth and induce the differentiation towards the lineage of

S. Caponi
Istituto Officina dei Materiali, National Research Council, Perugia, Italy

C. Canale · O. Cavalleri
Department of Physics, University of Genova, Genoa, Italy

M. Vassalli (✉)
Institute of Biophysics, National Research Council, Genoa, Italy
e-mail: massimo.vassalli@cnr.it

interest. A growing body of evidence suggests that the most affordable way to design an effective scaffold is to exploit a biomimetic approach, trying to emulate the characteristics of the natural environment. Moreover, it has been pointed out that not only the chemical nature of the material is relevant to this process but also its physical and, in particular, mechanical properties. Mapping the elasticity of a living tissue is becoming more and more relevant in the rational design of next generation biomimetic scaffolds, and the exploitation of advanced tools is required to achieve sub- μm resolution, comparable to the length scale probed by a single living cell.

2 Introduction

Living beings are studied in the context of life science from different points of view, but they can also be observed from an engineering perspective. Having survived millions of years of evolutionary pressure, living organisms have developed very specialized and effective behaviors and structures that can be regarded as an efficient template for the rational design of advanced engineering solutions. Smart textiles [52], visionary buildings [44], or locomotion strategies for swimming robots [42], all are examples of such a biomimetic approach, but the field of science that more inherently benefits of this strategy is probably biomedical engineering and, in particular, tissue engineering and regenerative medicine (TERM) [63].

The aim of TERM is to assemble functional constructs able to recover failing tissues or whole organs. After more than 30 years of intense research activity over the world [116], some engineered tissues have been fully translated to medicine and approved for human application [51]. Nevertheless, complex organs, such as liver, pancreas, or kidney, are still out of reach for current approaches and an extremely vital community is working to address the main issues of current methodologies in TERM [56].

The main experimental approach, emerging as a de facto standard in TERM, requires the development of biomimetic materials able to harness the self-healing potential of the organism [28]. Engineered scaffolds mimicking the natural physical and chemical environment can be designed to induce a local recruitment of undifferentiated cells and to elicit the formation of neotissue of the desired type [90]. Single cells, in particular stem cells, are extremely dynamical, continuously adapting to the matrix they are embedded in, deciphering and reacting to the mechanical and chemical cues provided by the material [49]. To guide their behavior, effectively inducing the desired response, it is of paramount importance to finely control the properties of the local microenvironment [11, 120].

The technological challenge posed by modern TERM is the development of characterization tools able to measure the material properties of the original (healthy) tissue and the corresponding engineered scaffold on a sub- μm length scale. This is particularly true when the biomechanical properties of the scaffold are concerned. Stem cells feature a panel of sensors to interpret the mechanical environment, either exploiting mechanisms occurring at the boundary of the cell,

the membrane [7], or involving the whole cell body [106]. These cellular machineries are able to trigger several transduction pathways, influencing the cell phenotype and eventually inducing stem cells differentiation towards a specific lineage, depending on the local elasticity [37]. In order to design an optimal scaffold for TERM application, specifically tailored to direct stem cell phase, it is mandatory to accurately know and control the mechanical properties of the material [62].

The availability and effectiveness of nanotechnology tools to characterize mechanical properties of biological materials has been widely reviewed during last years [13, 14, 82] and the potential application to biomimetic materials has also been investigated [49]. In this chapter, we recapitulate the main state-of-the-art methods to physically map the mechanical properties of biological materials, emphasizing approaches able to achieve sub μm resolution (Sect. 3.1) and concentrating on some key research findings in the context of rational design of biomimetic materials (Sect. 3.1). Moreover, we will also present new and emerging noncontact mechanical imaging technology (Sect. 3.2), able to achieve unprecedented resolution and thus provide a potentially breakthrough contribution to the field (Sect. 4.2).

Finally, current limitations and future perspectives of in vitro biomechanical mapping will be presented, with a special attention to the translational potential towards biomedical applications (Sect. 5).

3 Experimental and Instrumental Methodology

Measuring the mechanical properties of a soft biological material can be generally obtained either exploiting contact mechanics or measuring the effect of local material properties on the propagation of a physical wave (remote mapping). Both approaches have been extended to achieve single-cell high-resolution sub- μm resolution, and they will be discussed in the next sections.

Indenting a material with a tip of known geometry while measuring the corresponding force is the standard approach to measure mechanical properties (either static or dynamic) of a material, and a robust literature exists to model and analyze the resulting experiments [80]. This approach has been translated to biological applications and scaled down to nanometer size by means of the so-called atomic force microscope (AFM). Section 3.1 will present the measuring principle and the specific implementation nowadays available on the market, while key applications of AFM mechanical mapping on living cellular systems and biological materials are reported in Sect. 4.

While the scaling down of standard nanoindentation approaches to the nanoscale mainly involves technological issues, the identification of a remote mapping method with sub- μm resolution also implies to overcome some physical limitations. In fact, remote elastometry, as deployed in medical context, is based on acoustic imaging that, even using recent super-resolution advancements, hardly goes under 1 mm [40]. Nevertheless, not only the propagation of sound is influenced by the material

properties of the medium but also light can be used to probe the local elasticity, and this is the topic of Sect. 3.2 in which the use of Brillouin spectroscopy to achieve high resolution elasticity mapping is presented.

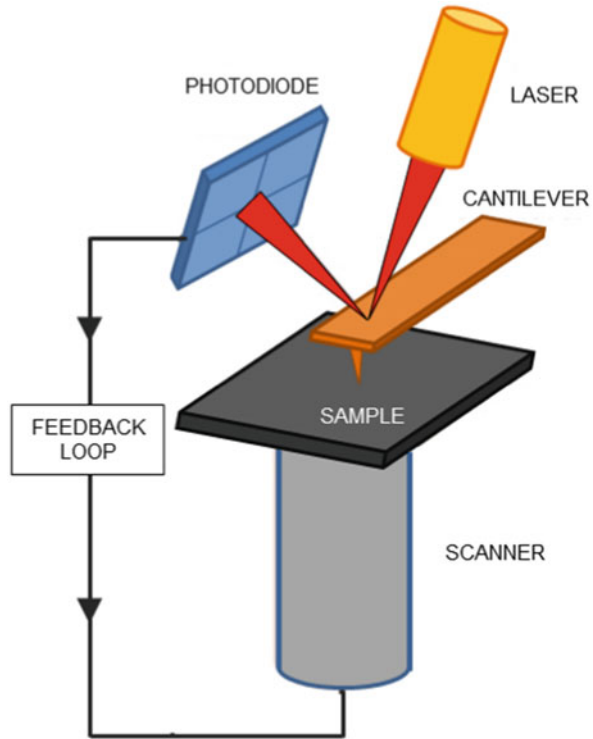
3.1 Scanning Probe Microscopy

Atomic Force Microscopy (AFM) is the second born member of the Scanning Probe Microscopy (SPM) family. The first scanning probe microscope, the Scanning Tunneling Microscope (STM), was invented in 1981 by Binnig e Rohrer [16]. Despite its extremely high spatial resolution, STM is not suitable for the analysis of biomaterials since it requires conductive samples. This limitation was overcome by the introduction in 1986 of the AFM [17] which can be used on insulating samples and is therefore well suited for the analysis of biological samples and bio-inspired materials. Other members of the SPM family followed over the years, like, to cite a few, Magnetic Force Microscopy (MFM) [48], Near-Field Scanning Optical Microscopy (NSOM) [12], and Scanning Thermal Microscopy (SthM) [130]. The key point of scanning probe microscopes is the use of a sharp tip which is placed in close proximity of the sample surface. The interaction between the tip and the sample is recorded while the tip scans over a selected area of the sample and the signal is used to build up a 3D image of the sample surface. In the case of AFM the signal of interest is the interaction force between the tip and the surface. As discussed below, AFM can be used not only as an imaging tool but also as a spectroscopic tool able to provide information on the mechanical properties of the samples under investigation.

3.1.1 The Microscope

A schematic of a typical AFM setup is shown in Fig. 2.1. The probe is based on a flexible μm -size cantilever fixed from one side and featuring a sharp tip at the free end. While the cantilever is scanned over the sample, the interaction force between tip and sample causes a deflection of the cantilever. The most commonly used method to measure the deflection of the cantilever is the so-called optical beam deflection method (OBDM). A laser beam is focused on the backside of the cantilever and the reflected beam is sent to a four quadrant photodiode. In this configuration, a deflection of the cantilever will cause a tilt of the reflected beam. Upon a proper calibration of the system, from the difference between the beam intensity on the upper and lower half of the photodiode the cantilever deflection can be evaluated, while from the difference between the beam intensity on the left and right half of the photodiode, the cantilever torsion can be evaluated. The high sensitivity of the optical method derives from the fact that the tip-photodiode distance is usually three order of magnitude larger than the cantilever length (millimeters vs micrometers), which greatly magnifies the tip displacements. When AFM is operated as an imaging tool, the tip is raster scanned over the sample (or the sample is raster scanned under the tip, depending on the microscope configuration) by using a piezoelectric scanner, which allows an extremely accurate motion of the

Fig. 2.1 Schematic diagram of a probe-scanned AFM including the main components

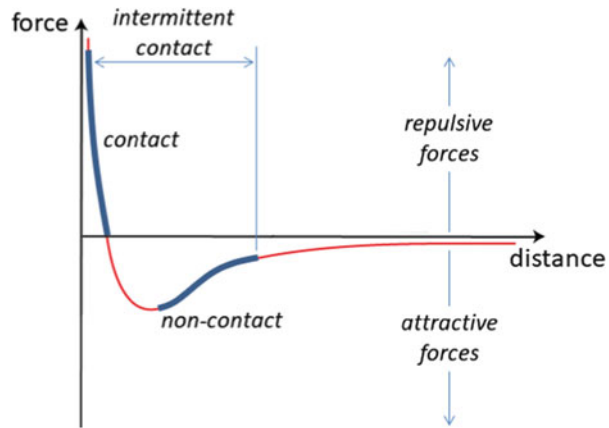


tip relative to the sample. The tip to sample distance, and therefore the interaction force, can be measured and controlled during scanning thanks to a feedback loop which tunes the position of the piezoelectric by changing its polarization.

3.1.2 AFM Operation Modes

The AFM can be operated in different modes, i.e., contact or DC mode and resonance or AC mode. In contact mode, the feedback system scans the AFM tip relative to the sample, with the tip kept in closest proximity with the surface and the static deflection of the cantilever is detected. In resonance modes, the cantilever is forced to oscillate at its resonance frequency and changes in its oscillation due to the interaction between the tip and the surface are detected. A schematic plot of the interaction force between tip and surface is reported in Fig. 2.2. In contact mode, short-range repulsive forces are involved in the interaction, while in resonance mode, long-range attractive forces come into play. In contact mode, the AFM is usually operated at constant force: the feedback loop modulates the z polarization of the piezo scanner in such a way to keep constant the cantilever deflection, i.e., the interaction force. The image is formed by recording the z polarization as a function of the (x,y) position of the tip and quantitative information on the surface morphology can be extracted from image analysis. The applied force, which can be modulated by the cantilever spring constant, can critically affect the image contrast,

Fig. 2.2 Schematic plot of the forces between tip and sample as a function of their distance. The regions of operation of the different imaging modes are shown



especially when soft samples like biological specimens are investigated. In this case, the use of very soft cantilevers and the possibility to image samples in liquid environment (to eliminate the effect of meniscus forces present in air imaging) can be successfully combined to achieve stable imaging on soft biological samples. By properly tuning the applied force it is even possible to switch from not perturbative soft imaging to high-load nanolithography modes [112].

Complementary information to sample morphology can be obtained in contact mode when the lateral force signal is recorded. As previously mentioned, the use of a four quadrant photodiode allows to monitor the torsion of the cantilever which is due to the friction between tip and surface. In this way, topographically uniform regions endowed with different chemical properties can be discriminated, as it is the case, for instance, of phase separated samples [122]. For the analysis of soft samples like biological ones, contact mode imaging can be advantageously complemented by resonant operational modes. In AC modes, the cantilever is oscillated close to its resonance frequency, depending on the cantilever oscillation amplitude and on the tip to surface distance intermittent or noncontact contact modes can be distinguished. As shown in Fig. 2.2, in intermittent contact mode, the tip oscillates from the contact region where it experiences repulsive forces to the noncontact region where it experiences attractive forces. The intermittent contact avoids the shear forces that the tip can exert on the sample in contact mode [27]. Images are formed by recording the piezo polarization signals set by the feedback loop in order to maintain selected cantilever oscillation amplitude. Very good vertical and lateral resolution can be achieved. Additional information on sample properties, like stiffness, viscosity, or adhesion, can be obtained by recording in a separate acquisition channel the phase difference between the cantilever oscillation and the driving signal [65]. Intermittent contact can be used in liquid, a favorable condition for biological or biomimetic samples. Noncontact mode differs from intermittent contact because during cantilever oscillation, the tip never touches the sample and experiences only long-range attractive forces; the oscillation amplitude is smaller than in intermittent contact. The interaction force between tip and sample is very low; this imaging mode is therefore

highly non perturbative, but the lateral resolution is lower compared to other modes. Further, noncontact can be operated only in air and, even on dry samples; because of the small-oscillation amplitude, the tip can be trapped by the thin condensed vapor layer on the surface.

3.1.3 Force Spectroscopy

Even if initially introduced as an imaging tool, over the years AFM has shown a huge potential as a spectroscopic tool, able to investigate at a very high-force resolution the interaction between the tip and the surface [25]. AFM spectroscopy can be exploited to get information on local chemical and mechanical properties like adhesion [81] or elasticity [83] as well as to investigate at the single-molecule level the interaction between specific molecular systems [79]. In the spectroscopic scheme, AFM is operated in a point mode, which means that the tip is not scanned over the surface, but, at a fixed lateral position, the cantilever deflection is recorded while the distance between tip and sample is changed from a large distance to contact and back to a large tip-sample separation. In this way a so-called force-distance curve is obtained. A general scheme is reported in Fig. 2.3. At large tip-sample separations, i.e., no interaction between tip and sample, the cantilever deflection is zero. Approaching the sample to the cantilever a point is reached when the gradient of the attractive force becomes larger than the cantilever elastic constant and the tip is captured by the sample, in the jump-to-contact point. The interaction force enters the repulsive regime and further approaching the sample results in larger cantilever deflections, with eventual sample indentation depending on the relative stiffness of the sample with respect to the cantilever. When reversing the sample displacement direction, the retraction curve is recorded. The sample is withdrawn until the tip is released from the surface, in the jump-off-contact point. Further retracting the sample from the jump-off-contact point, the tip-sample interaction vanishes and

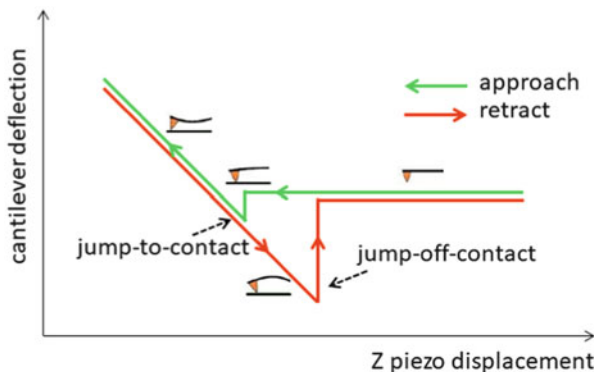


Fig. 2.3 Ideal Force-Distance (F-D) curve on a rigid sample. In the approach curve, starting from the right, the interaction between tip and surface is negligible until the jump-to-contact point, where the tip is captured by the surface. Moving further on, the deflection increases linearly in the contact region (rigid substrate). In the retract curve, the piezo is retracted until the tip is released from the surface in the jump-off-contact point

the deflection is zero. In order to derive quantitative data on interaction forces from the force distance curve, it is necessary to carefully calibrate the output of the photodiode system used to measure the cantilever deflection. To this end, a preliminary force curve has to be acquired on an ideally stiff sample (i.e., on a sample much stiffer of the cantilever used for the measurements). Under these conditions, the contact region of the curve must be linear with a unitary slope. Provided the piezoelectric scanner is properly calibrated, from the analysis of the preliminary curve, the photodiode signal can be converted into cantilever deflection calibrated values. In order to convert deflection values into force values through the Hooke's law:

$$F = -k\Delta z \quad (2.1)$$

the cantilever spring constant k has to be known. Nominal cantilever spring constants are provided by manufacturers, but for more accurate force evaluation, a direct measurement of the spring constant is desirable. Among the different methods, the thermal noise approach can be used to evaluate k [50].

3.1.4 Determination of Solid Elasticity by AFM Indentation Experiments

In the last two decades, the AFM in force spectroscopy mode has been widely employed in the analysis of the elastic/mechanical properties of biomaterials. By using soft cantilevers, materials with elastic moduli below 1 kPa can be tested. The AFM is able to discriminate variation of the local elasticity with a lateral resolution imposed by the tip size, hence, close to the molecular scale. In a typical indentation experiment, the AFM probe is pushed on the tested materials until the cantilever deflection reaches a pre-defined value (deflection setpoint). Increasing the applied force, the AFM probe gradually starts inducing a deformation of the sample (indentation). The shape of the resulting force versus distance curve contains information on the mechanical properties of the sample that should be further unravelled and quantified. After a tricky filtering and preprocessing phase (see [61] and Sect. 3.1.3), the force versus indentation experiment can be fitted on the expectations of a relevant descriptive model, to identify the corresponding material properties. Although different approaches have been proposed for AFM data interpretation [60], so far the most adopted model is based on the simple Hertz contact mechanics [123], eventually in the generalized Sneddon form that takes into account nonspherical indenters [111]. The Hertz model is theoretically valid under very special conditions, so that the sample could be treated as an isotropic and linear elastic body (viscous or plastic effects must be minimized), occupying an infinitely extended half plane (far larger than the tip size). Even though these requirements are considerably stringent, the Hertzian mechanics provides a reliable and effective first-order approximation of the mechanical properties of a biomaterial and special cases (such as thin layers or patterned substrates) can be treated as corrections to the general formulation (see Sect. 4.1 and [33]).

If the force F is measured as a function of the vertical displacement Z , as in an AFM experiment, it is possible to obtain the force versus indentation curve $F(\delta)$ by

taking into account the position Z_0 at which the tip contacts with the sample (contact point) and the resting deflection x of the cantilever during the penetration:

$$F(Z) \rightarrow F(\delta) \quad (2.2)$$

$$\delta = Z - Z_0 - x = Z - Z_0 - \frac{F(Z)}{\kappa} \quad (2.3)$$

where κ is the elastic constant of the cantilever (see Sect. 3.1.3). A generalized mechanical response can be expected in the form:

$$F = E^* \rho \delta^\beta \quad (2.4)$$

where E^* is the reduced Young's modulus accounting for the Poisson ratio:

$$E^* = \frac{E}{(1 - \nu^2)}$$

and ρ and β broadly depend on the indenter geometry; in the original Hertz theory of a spherical indenter of radius R , these parameters can be calculated as:

$$\rho = \frac{4}{3} \sqrt{R}; \beta = 3/2$$

while, in the conical approximation (more suitable for an AFM tip) if α is the apex aperture angle, the same parameters read as [111]:

$$\rho = \frac{2}{\pi} \tan \alpha; \beta = 2$$

3.1.5 AFM-Based Mechanical Mapping

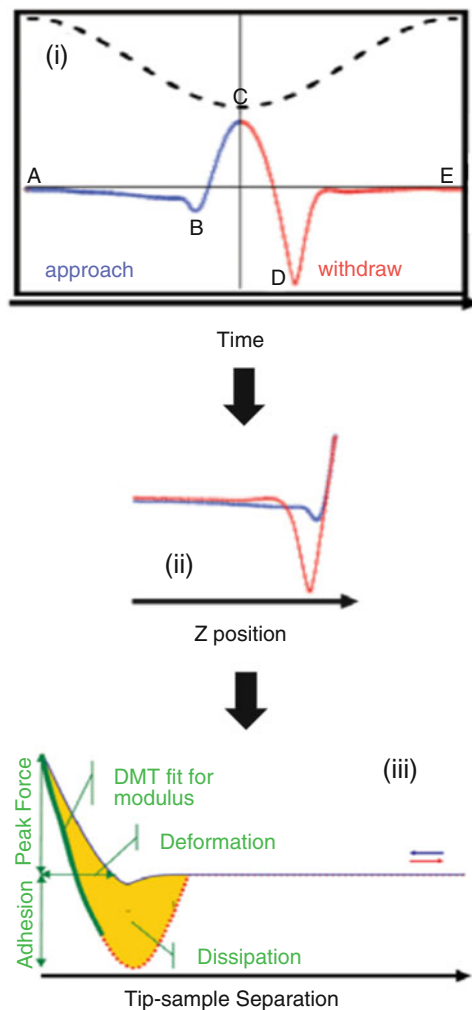
In the previous paragraph, we show how the AFM can be employed in the determination the local elastic properties of new materials for biomedical applications. In particular, we show how it is possible to work on small objects or to focus the analysis on a confined portion of the material. In spite of this, we didn't present any map of elasticity with a lateral resolution comparable with the typical lateral resolution of the AFM imaging mode. In the last decade, new technological approaches allowed for the acquisition of maps of elasticity formed by hundreds of thousands of points in a reasonable acquisition time. By using this new modalities, it is possible to obtain a distribution of elasticity that perfectly correlates with the topographical view of the sample, this means, on the exactly same area and with the same number of points. This technique paves the way for a new correlative approach in which all the feature displayed in the topography are also describe in terms of elasticity.

Among all the mechanical mapping approaches, one of the most successful implementations is the so-called PeakForce Tapping mode, marketed by Bruker since

2010. Here this technique will be briefly described and some application presented. PeakForce QNM is the further development of the pulsed force mode introduced some years in advance [92]. In PeakForce QNM mode, and similarly to Tapping mode, the AFM tip and the sample are intermittently brought in contact for a short period, minimizing the lateral forces (Fig. 2.4, see also Sect. 3.1.2). PeakForce is a dynamic mode, but unlike the traditional AC mode, PeakForce controls the position of the piezo to keep constant the maximum force (Peak Force) on the probe, instead of the vibration amplitude.

PeakForce QNM AFM mode allows the acquisition of maps of elastic modulus of a sample surface working as fast as standard tapping AFM imaging, i.e., acquiring a 512×512 points map in some minutes. The elastic modulus is calculated from the

Fig. 2.4 (a) A force curve is captured per each modulation cycle. The dashed line represents the Z-position of the piezo along a single period of the modulation. The solid line represents the measured force on the tip when the probe is approaching the sample (blue), and when the probe is moving away from the sample (red). Both quantities are plotted as a function of time. The point B is the jump-to-contact, C is the maximum applied force, controlled by the feedback loop, i.e., the peak force, while A is the maximum adhesion between tip and sample. (b) when the force is plotted as a function of the Z-displacement, the typical aspect of a force-distance curve is displayed. (c) The fit with the DMT model is performed on Force vs. Separation curves. The separation is calculated considering the Z-piezo position and the cantilever deflection [39].



force-indentation curves by using the Derjaguin-Muller-Toporov (DMT) model (Fig. 2.4) [113]. The PeakForce mode is capable of working with very small load forces, up to 0.1 nN, applying very small indentation depths, up to 1 nm. This unique feature of PeakForce makes the modality particularly suitable in the study of thin materials. PeakForce QNM is able to quantify Young's moduli in the range between 0.7 MPa and 70 GPa. To better exploit its capability, the choice of the cantilever is fundamental. In nanomechanical investigations, the maximum sensitivity is reached when the spring constant of the cantilever is equal to the effective spring constant of the sample [113]. When the spring constant of the cantilever is one order of magnitude higher or lower than that of the sample, the sensitivity is three times lower. For this reason, a rough estimate of the sample stiffness is important to set the correct experimental configuration. Here two examples on sample characterized by significantly different stiffness are reported.

Smolyakov and co-workers [110] investigated the nanomechanical properties of chitin-silica hybrid nanocomposites, employing stiff cantilever with a nominal spring constant $k = 200 \text{ N/m}$ to optimize the sensitivity of their experimental setup for Young's moduli in the order of the GPa.

Moreover, Sweers et al. [113] used cantilevers with a $k = 27 \text{ N/m}$ to test amyloid fibrils from α -synuclein, a biological material, but characterized by high-mechanical resistance (see Fig. 2.4a). In Fig. 2.5, the typical elasticity map of chitin nanorods deposited on silica substrate is shown. However, measuring the elasticity of objects with a cross-section in the order of few tens on nanometers is still challenging. In particular, the modulus significantly changes across the nanorod. An example of this variation is reported in Fig. 2.5b, while a cartoon explanation is provided in Fig. 2.5c. When the tip comes in contact with the nanorod side (in Fig. 2.5a the scan direction is from right to left), the contact is not spherical, and the DMT model is not applicable. Furthermore, the radius of contact is not correct in this case. Generally, these deviations from the ideal conditions bring to an overestimation of the elastic modulus. This artifact is called "edge effect." On the opposite side of the nanorod, an area is not accessible to the tip, due to the specific direction of its movement. This area is not tested; the authors called this area "shadow effect." Edge and shadow effects are present also inverting the scan direction, confirming the validity of the geometrical interpretation proposed by Smolyakov et al. [110]. The minimum value of the modulus, corresponding to the central area of the nanorods (see Fig. 2.5), was considered as the nanorod modulus, assuming that this value is less affected by geometric artefacts. The authors found a different behavior in the mechanical properties of textured chitin and chitin-silica films, measuring in both cases elastic moduli in the order of the GPa and optimizing the experimental condition in the study of these kind of samples.

Edge and shadow effects are also present in the elasticity maps acquired by Sweers et al. and clearly displayed in Fig. 2.5e, f. In this image, the mica background elastic modulus is underestimated, being about 1.5 GPa. This is likely due to the limited range of elastic moduli which can be explored by the cantilever employed in the work, demonstrating again the key role played by the probe in the PeakForce QNM mode.

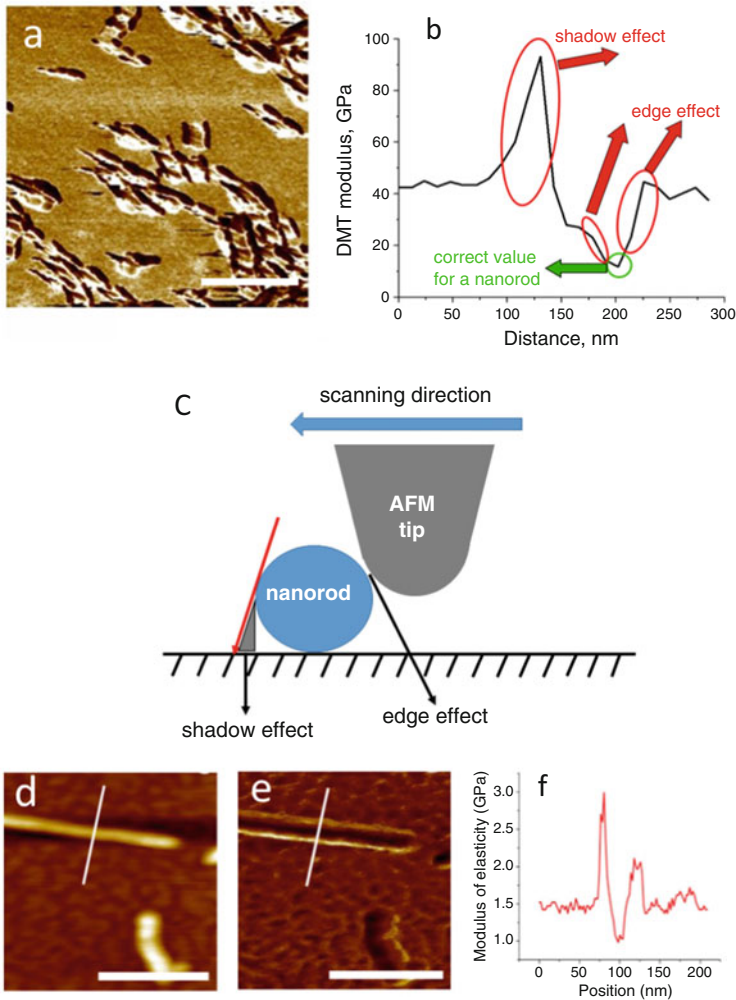


Fig. 2.5 (a) Maps of Young's modulus of chitin nanorods on silica substrate. The modulus image by PeakForce QNM ($3 \times \mu\text{m}^2$) was obtained by using a peak force of 150 nN. (b) Modulus variation along nanorod cross-section along the scan direction. (c) Graphical explanation of the artifacts induced in the modulus determination by edge and shadow effects.

3.2 Brillouin Spectroscopy

Brillouin light scattering (BLS) is a spectroscopic technique able to access the viscoelastic properties of the materials in the GHz frequency range.

For many years, this technique has been largely exploited in material science and condensed matter physics [26, 30, 32, 108, 118], but recently, thanks to its non-invasive character, new applications fields started to be explored [19, 54, 73].

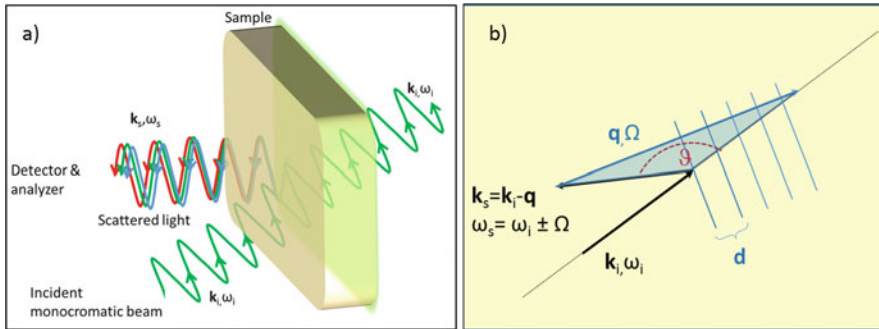


Fig. 2.6 (a) Schematic picture of inelastic light-scattering process. The incoming beam of given wave-vector \mathbf{k}_i and frequency ω_i interacts with the internal normal modes of the sample and diffuses in the space changing its frequency ω_s and wave-vector \mathbf{k}_s . The position of the analyzer fixes the scattering geometry. (b) Schematic picture of spontaneous Brillouin scattering process. The presence of sound wave in the sample of wave-vector \mathbf{q} and frequency Ω , shown as a series of parallel lines, induces the diffusion of the incoming monochromatic beam. In the scattered light, besides the incident frequency, two other components with frequency $\omega_s = \omega_i \pm \Omega$ and wave-vector \mathbf{k}_s are present. The scattering geometry is defined by the scattering angle ϑ , the angle between the vectors \mathbf{k}_i and \mathbf{k}_s on the scattering plane.

BLS is based on the inelastic scattering of photons from the long-wavelength acoustic phonons (~ 200 nm) naturally present at thermodynamic equilibrium in any material [32].

The interaction between light and the sound waves gives rise to the so-called Brillouin scattering, in honor to Leon Brillouin who first described this effect at theoretical level, almost a century ago [21].

In a typical BLS experiment, as schematized in Fig. 2.6a, a monochromatic beam of a given frequency ω_i and wave-vector \mathbf{k}_i is incident on a medium, whose spatial and temporal fluctuations of the local dielectric constant are responsible of light scattering processes [10, 29]. In particular, the light diffuses changing its wavevector when it goes through an optically heterogeneous material, if the material's heterogeneities are also time dependent, the light will change also its frequency.

Let us consider, for example, the inelastic light scattering generated by a 3D crystalline material; if p is the number of ions in the unit cell, we expect $3p$ normal vibrational modes: three of them are acoustic modes, one longitudinal (LA), and two mutually perpendicular transverse (TA1, TA2), the others $3(p - 1)$ are optical modes. All of these vibrations can induce dielectric constant fluctuations able to cause light scattering. In particular, if the scattering is generated by the propagating *acoustic waves* the process is called *Brillouin Light Scattering*, while if it is generated by optical modes, the process is called *Raman scattering*. Although these two spectroscopic techniques do not differ from the conceptual point of view, probing different frequency ranges, they have been developed as separate experimental methods able to obtain complementary information on mechanical and chemical properties of the materials, respectively.

In the following, we will focus on the Brillouin Light Scattering process, analyzing how it can represent a powerful tool to characterize the elastic constants in materials of biological strategic interest.

Let's consider a normal vibrational mode of wave-vector \mathbf{q} and frequency Ω . Avoiding the description referring to the microscopic structure of the material, the normal vibrational mode can be described as a wavelike modulation in a continuous medium. As schematized in Fig. 2.6b, at any given time, a density modulation with a periodicity $d = 2\pi/q$ is associated to the considered vibrational mode and can be regarded as a diffraction grating. The incoming light beam of frequency ω_i and wave-vector \mathbf{k}_i will diffuse approaching this grating with a well-defined wavevector given by the Bragg's law $2d \sin(\vartheta/2) = 2\pi m/k_s = 2m\pi/k_i$ (with m an integer), i.e., for $m = 1$ $q = 2k_i \sin(\vartheta/2)$ since $|\mathbf{k}_i| \sim |\mathbf{k}_f|$.

In the case of propagating acoustic modes, the density modulation moves in time with a constant phase velocity given by

$$v = \Omega/q \quad (2.5)$$

So the collective vibrations have to be considered as a moving diffraction grating in the material. The time evolution of the diffraction grating maintains unaltered the orientation and the distance d between two successive planes, conserving the relation 2.5 on the wavevector. On the contrary, the frequencies of the scattered light, ω_s , will be affected by the grating motion undergoing to the Doppler effect, i.e.,

$$\omega_s = \omega_i \pm \Omega \quad (2.6)$$

Brillouin light scattering process can be also explained from quantomechanical point of view, using corpuscular description. Considering the "photons" and the "phonons" as virtual particles corresponding to the normal modes of radiation field and ionic displacement field, respectively, the scattering process can be schematized as a photon-phonon collision. Imposing the conservation of energy, the relations in Eq. 2.6 are again obtained. Moreover imposing the conservation of the momentum, the relation

$$\mathbf{k}_i - \mathbf{k}_f = \pm \mathbf{q} \quad (2.7)$$

can be written.

Being $|\mathbf{k}_i| \sim |\mathbf{k}_f|$, the triangle highlight in Fig. 2.6b is nearly isosceles and the exchange wave-vector of the process will be $q = 2k_i \sin(\vartheta/2)$ where ϑ is the angle between \mathbf{k}_i and \mathbf{k}_f . It is worth to notice that the existence of the sign \pm in Eqs. 2.6 and 2.7 are linked to the phonon creation or annihilation.

Analyzing the frequency of the scattering light, two contributions have to be expected, i.e., the Stokes and anti-Stokes components of the Brillouin doublet, symmetrically shifted with respect to the elastic line at frequency $\pm \Omega$, respectively.

Moreover, considering that the modulus of the exchange wavevector q is of the order of 0.02 nm^{-1} , value very small compared to the typical dimension of the Brillouin zone ($\sim 10 \text{ nm}^{-1}$), the process gives information only for the long wavelength phonons for which (i) the linear dispersive relation as well as (ii) the approximation of the sample to continuous medium are well verified. Thus, by measuring the frequency shift of a scattered light, it is possible to achieve the local speed of sound v of the collective vibration which generated the scattering process.

Of course, the described effect occurs for each collective acoustic vibration present in the material. So, for example, the Brillouin spectrum of a 3D cubic crystal will be composed by three Stokes and three Anti-Stokes peaks. Measuring their frequency position, it is possible to estimate the longitudinal and the two transversal sound velocities characterizing the elastic tensor of the sample [117].

3.2.1 Elastic Constants Probed by BLS

If three independent monochromatic plane waves describe the collective oscillations in a 3D cubic crystal, in isotropic crystals (or amorphous materials), the symmetry relations reduce the number of independent elastic constants.

The transverse modes collapse one to the other, so the expected characteristic Brillouin spectrum is composed by two Stokes and two anti-Stokes peaks, symmetrically shifted with respect to the elastic line at frequencies:

$$\Omega_L = qv_L = q\sqrt{\frac{\left(B + \frac{4}{3}\mu\right)}{\rho}} = q\sqrt{\frac{M}{\rho}}$$

and

$$\Omega_T = qv_T = q\sqrt{\frac{\mu}{\rho}}$$

where Ω_L and Ω_T are the frequency position of the longitudinal and the transversal Brillouin peak, respectively, ρ is the mass density, B the bulk, and M the longitudinal and μ the shear modulus. The shape of the Brillouin spectrum will change due to the presence of particular selection rules related to the scattering angle ϑ , to the polarizations of both photons and phonons and to their relative orientations with respect to the scattering plane.

In general, the Brillouin scattering process is characterized by a low cross section. Furthermore, considering the low-frequency shift of the scattered light respect the elastic one $\Omega = \omega_s - \omega_i$ (in the range between 3 to 30 GHz in soft matter), high-resolution and high-contrast spectrometers are necessary to detect the tiny inelastic Brillouin signal. Different experimental set-ups are nowadays designed to achieve a good signal quality and in the following we describe their main features considering advantages and disadvantages of the more common types.

3.2.2 Experimental Set-up for Brillouin Scattering Experiments

After lasers advent, inelastic light scattering set-ups have been developed using spectrometers or interferometers able to detect the small-frequency variation (tens of GHz) and the weak intensity of the Brillouin signals (typically several orders of magnitude weaker than the elastic Rayleigh peak). In material science and condensed matter physics, the widest used instrument is the tandem Fabry-Pérot interferometer (TFP), in particular the 6-pass tandem Fabry-Pérot developed in the 1970s by John R. Sandercock [19, 26, 30, 108]. Its performance increased during the last two decades, and the last upgrade named TFP-2 HC, developed a few years ago, has drastically improved the set-up performance, widening the range of investigable samples. The internal optics of the instrument has been deeply modified obtaining an unprecedented contrast together with a high-frequency resolution (around 100 MHz). The contrast is the key parameter which defines in interferometric systems the peak-to-background ratio. The TFP-2 HC yields an instrumental contrast better than 150 dB [70, 103] opening the way for Brillouin scattering to study highly opaque or turbid media such as tissues of medical biopsies [68], biofilms grown on a metallic substrates [69, 103], or single living cells adhering to silicon slabs [70].

A recent proposed alternative to the TFP interferometer is offered by the VIPA (virtually imaged phase array) apparatus (a picture is shown in Fig. 2.7).

Using a nonscanning method for the light dispersion, VIPAs doubtless increase the acquisition speed of the spectrum allowing fast Brillouin imaging. However, several limitations characterize their use: the thickness of the etalon determines the spectral resolution which is limited to ~ 0.7 GHz and the spectral range restricted to some tens of GHz. Nevertheless, the most severe limitation is the low contrast which reaches the value of 30 dB in the single-pass setup. Different strategies have been developed to increase the VIPA contrast in order to detect the Brillouin signals: the use of equalization technique [5] or the multipass configurations [99], also in combination with a triple-pass Fabry-Pérot interferometer as a bandpass filter [41] or notch filters [71]. With these approaches, the spectral contrast reaches values good enough to allow the Brillouin scattering measurements of transparent or moderately turbid media [5, 41].

Anyway, whatever device is chosen, the most used experimental configuration is the backscattering geometry, i.e., $\vartheta = 180^\circ$ in which, even if the selection rules avoid the presence of the transverse mode in the spectrum, the light absorption of non-transparent samples does not prevent the focalization and the detection of the scattered light. Moreover, a relevant advantage of the back-scattering configuration is the possibility to use a microscope as focalizing and collecting optic. At $\vartheta = 180^\circ$, the maximum exchanged wave-vector $|q|$ is reached. In this condition: (i) the Brillouin peak associated to the longitudinal acoustic mode reaches the greatest frequency shift from to the elastic line, $\Omega_L = v_L q$, becoming more easily measurable also in the presence of high elastic scattering and (ii) the error in the evaluation of the exchanged wavevector, q , due to the finite dimension of the collection lens reaches its minimum value. This last condition allows the use of collection optics with high

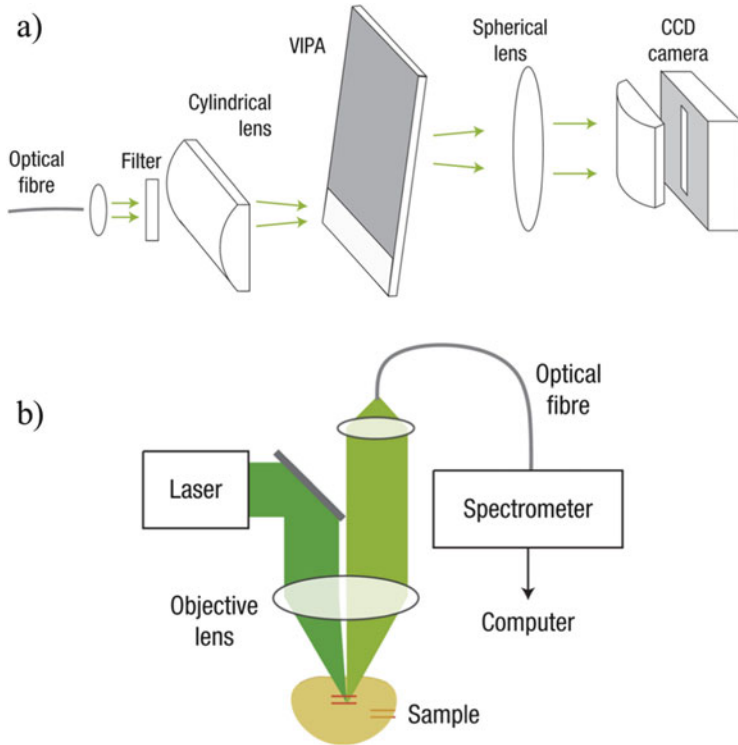


Fig. 2.7 VIPA-based optical setup: (a) Experimental setup of a single-stage VIPA spectrometer. (b) Schematic of the confocal Brillouin microscope system. (Reprinted with permission from [98])

numerical aperture, as microscope objectives, because the lineshape deformations are minimized [3]. However, also in backscattering condition, to analyze the Brillouin peak and in particular to correctly estimate its width, the asymmetric broadening related to the use of high numerical aperture objectives has to be taken into account [70].

The recent developments of Brillouin microscopes allow to measure the elastic properties of heterogeneous materials with a sub-micrometric spatial resolution, paving the way for high resolution mechanical imaging [5, 36, 53, 98, 104]. An innovative all-optical approach has been recently optimized in order to obtain the micro-mechanical analysis correlated with the local chemical composition [70, 73, 103, 115]. This approach has proved particularly useful for characterizing spatially heterogeneous materials such as biological cells and tissues. The inelastic light scattered from the same scattering volume is collected by a microscope and simultaneously analyzed by a Brillouin and a Raman spectrometers. The experimental set-up composed by a High-Contrast tandem Fabry-Pérot interferometer and a Raman spectrometer is reported as an example in Fig. 2.8.

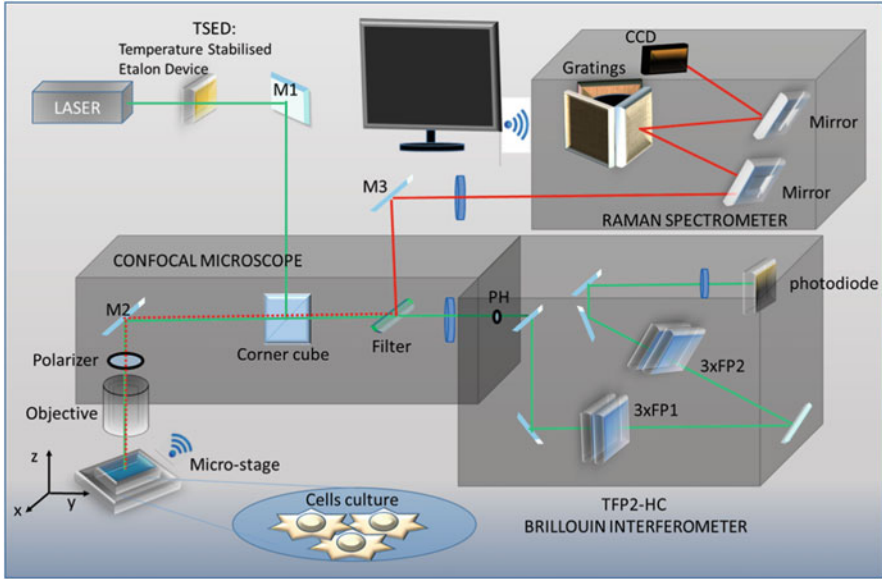


Fig. 2.8 Layout of the experimental setup composed by a High-Contrast tandem Fabry-Pérot interferometer (TFP-2 HC) and a Raman spectrometer. The laser beam is focused onto the sample by the same microscope objective used to collect the backscattered light. A short-pass tunable edge filter transmits the quasi-elastic scattered light (green beam) to the Brillouin spectrometer and reflects the inelastic scattered light (red beam) towards a Raman monochromator. Reprinted with permission from [70]

3.2.3 Key Time and Length Scales Probed by Brillouin Scattering

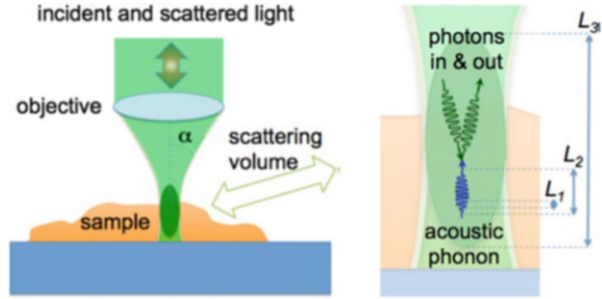
While planning a Brillouin experiment or comparing its results with those obtained by other techniques, a particular attention has to be paid to the relevant length and time scales probed by the spectroscopic approach.

In fact, being BLS an optical tool which directly probes material phonons, three different length scales have to be considered to explain the spectral shape and to estimate the effective spatial resolution obtained in the mechanical characterization [68, 70].

As schematically reported in Fig. 2.9, the smallest relevant length scale is represented by the wavelength of the probed acoustic modes, L_1 , which, in a typical light scattering experiment, is of the order of $\sim 0.1 \mu\text{m}$.

Elastic inhomogeneity much smaller than L_1 are not measurable from the acoustic field, which instead is sensitive to a mean value over the phonons wavelength. However, the presence of elastic spatial inhomogeneities of the order of $L_1/10$ or larger gives rise to the acoustic scattering effect, which in turn affects the propagation of the phonons and the Brillouin spectral shape. Their effect is well characterized in amorphous and porous glassy systems [22–24]: it originates attenuation processes of the acoustic field and anomalous dispersion of the acoustic modes [67].

Fig. 2.9 Schematic representation of the characteristic length scales in BLS. (Reprinted with permission from [68])



The second intermediate length scale to consider is the so-called mean free path of the acoustic modes. In fact, in non-crystalline materials, phonons cannot be considered as propagating plane waves any longer, but they are damped oscillations with a characteristic life time. The propagation length of acoustic phonons, L_2 , principally depends on two different factors: (i) the morphological disordered structure of the investigated material, responsible of the “static attenuation process” and (ii) the microscopic processes active in the materials associated to energy exchanges with the vibrational modes (dynamical attenuation processes). Due to the different origin of attenuation processes, L_2 can vary significantly among different materials, even spanning several orders of magnitude [9, 23, 74, 119]. However, as far as the investigation of biological samples is concerned, it has to be mentioned that the characteristic L_2 values measured in dry tissues [68], in living cells immersed in their buffer solution [70], or in extracellular matrix structures [85] are of the order of $\sim 1 \mu\text{m}$. So we refer to this value for L_2 in the following.

Finally, the last length scale L_3 takes into account the sizes of the scattering volume, i.e., the part of the sample enlightened by the laser beam and from which the scattered light is analyzed by the interferometer reaching the photo-detector. In the usual Brillouin configuration, L_3 is $\sim 10 \mu\text{m}$, but it can be reduced by almost one order of magnitude $L_3 \sim 1 \mu\text{m}$ in the more stringent confocal condition of the Brillouin microscopy. In spatially heterogeneous materials, such as cells or tissues, the scattering volume can be composed by homogeneous sub-regions with characteristic size greater than L_2 and characterized by different elastic constants. In this case, the measured spectrum is composed by the sum of the Brillouin peaks originating from the different subregions. As measured in living fibroblast immersed in their buffer solution, if the spectral spacing between the Brillouin peaks is larger than their width, the different contributions can be separated [70] obtaining the mechanical characterization of each subregion. Otherwise, the frequency position of the Brillouin peak will be a mean value between those of the subunits and an heterogeneous broadening characterize the width of the peak as measured in dry brain tissues [68]. From this simple analysis, it appears that the spatial resolution limiting the Brillouin mapping is L_2 since the acoustic modes would make an average of the mechanical properties over such a distance.

The second pivotal parameter for the understanding of the elastic moduli obtained by BLS is the frequency range analyzed by the technique. In fact, in the case of viscoelastic materials, the time scale plays a key role in the evaluation of their mechanical response.

Being a GHz spectroscopy, Brillouin probes the materials at higher frequency respect to AFM, quasistatic tensile testing or ultrasonic measurements. Comparing the high and the low frequency behavior for different biological materials such as collagen and elastin for the extracellular matrix proteins [31, 35], living fibroblast for cells [102] and the crystalline lenses and cornea for tissues [101], the existence of a dual biomechanical scale emerges from the measurements. In the GHz frequency region, the characteristic values of the elastic moduli are in the GPa range, while investigating these systems in the lower frequency range their value drastically decreases.

The reason for these apparently conflicting results is twofold.

- (i) From one hand, the different techniques probe different elastic moduli. In fact, Brillouin spectroscopy probes M , the longitudinal elastic modulus, defined as the ratio of axial stress to axial strain in a uniaxial strain state, i.e., the material deformation is limited only on the unique axis considered. On the contrary, probing the Young's modulus, the material deformations are allowed also in the others directions respect to one of the axial stress. It is worth to notice, however,, that a strict correlation between the elastic moduli obtained in the high (GHz) and low frequency (quasi-static or kHz) range has been obtained both in tissues and cells [35, 101, 102] proposing the existence of a scaling law (see Fig. 2.10).

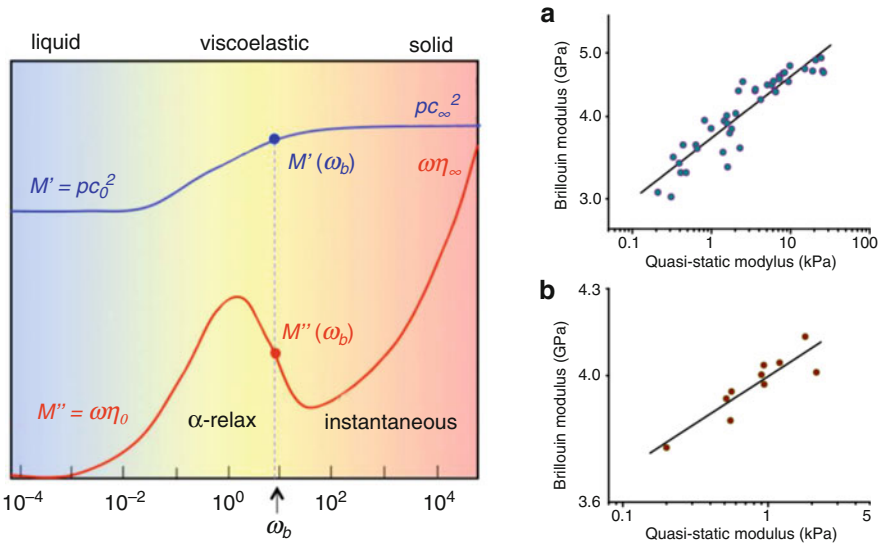


Fig. 2.10 Right panel: $M(\omega)$ behavior for the real (blue line) and an imaginary part (red line). The first one is related to the dispersion while the second to the absorption of the acoustic modes. ω_B indicated in figure is the frequency probed by the Brillouin techniques. Depending on the position of relaxation with respect to the frequency ω_B , different scenarios opened in the relation between $M'(\omega_B)$ and $M''(\omega_B)$. (Reprinted from [68]). Left panel: Comparison of Brillouin longitudinal and quasi-static Young's moduli for porcine lenses (a) and bovine lenses (b). Circles, experimental data; solid line, log-log linear fit. (Reprinted from [101])

This experimental observation, which deserves an in-depth phenomenological and theoretical investigation, confirms that both the techniques are sensitive, even if differently, to the same elastic modulations validating both as powerful tools for the biomechanics characterization.

- (ii) On the other hand, the elastic response of any viscoelastic material is strongly frequency dependent. This effect is largely characterized, for example, in glass forming materials [30, 57]. When a system undergoes the glass transition, its dynamics changes from the liquid-like behavior to the solid one increasing by orders of magnitude its viscosity and elastic moduli. Depending on the probed frequency range ω , the glass forming system appears as a liquid or as a solid. The characteristic frequency separating the two regimes is given in terms of the structural relaxation time τ_α , which is characteristic of any given material and changes its value as a function of temperature, pressure, or chemical modifications of the investigated sample. The structural relaxation defines the time scales which regulate the cooperative rearrangement processes by which the local structure reaches a new equilibrium after being perturbed.

Applying an external force or following the response to the spontaneous fluctuations in the low-frequency regime $\omega\tau_\alpha \ll 1$, the liquid-like behavior dominates: the system is able to follow the perturbation and it is in the so-called relaxed condition. On the contrary, when $\omega\tau_\alpha \gg 1$, the system is no more able to follow the time evolution of the perturbation. In this “unrelaxed state,” it shows a solid-like dynamics characterized by high viscosity and high elastic constants. A widely used approach to describe this behavior is introducing frequency dependence in the stress-to-strain relation which in the appropriate limits converges to the standard equations for a solid and a fluid [133].

In the generalized hydrodynamics framework, a complex frequency-dependent viscoelastic modulus is considered. The characteristic frequency behavior normalized to that of the α -relaxation is reported in Fig. 2.10 for the longitudinal elastic modulus $M(\omega)$ [18, 30]. To keep the model as simple as possible, we limit our discussions to the effect of the structural (or α -) relaxation process, neglecting the other relaxations eventually present in the system whose effect is described elsewhere (see for example [30]).

From the mechanical point of view, cells and tissues have been recently modelled as soft condensed matter near the glass or jamming transition [38, 64, 93, 94, 128]: the frequency dependence of their elastic moduli is a further confirmation of their similarity to glass forming materials.

4 Key Research Findings

Modern tissue engineering is exploiting the capability of new biomimetic materials to mediate cell response. An ideal biomimetic material is obtained by tuning not only the chemical and morphological but also mechanical properties of the material itself.

In particular, the development of soft tissue regeneration demonstrated that an effective physiological-like environment also requires the presence of physiological like mechanics. For example, the tuning of physical properties such as stiffness and topography has been used to control adsorption of specific proteins [75], driving the adhesion of monocytes and the polarization of macrophages. For drugs release purpose, the deformability of polymeric carriers is associated with a decreased recognition and interactions with specific cells of the immunosystem, thus to a reduction of their internalization and degradation [83]. Working on stem cells, field has been demonstrated that the mechanical properties of the extracellular matrix (ECM) regulate not only cell spreading but also the change of phenotypes in stem cells [127]. This limited number of examples, among the thousands in literature, is enough to demonstrate that the mechanical properties of a material are important, as much as the chemical and morphological properties, to define its interaction with biological cells. The characterization of biomimetic materials required the use of sensitive techniques, able to evaluate the mechanical properties of the material over a large range of elastic moduli, spanning from the GPa to the few hundreds of Pa, depending on the application, and possibly working in a physiological environment.

4.1 Indentation Experiments on Hard/Soft Materials

As already pointed out, single cells are able to sense local modulations of the mechanical properties, and the length scale on which this process occurs is comparable with single cell size (few μm) or even smaller. For this reason, in the last decades new materials have been proposed in which the mechanical properties were finely controlled at the microscale [45] or even at the nanoscale [109]. The leading characterization tool in this context is by far the AFM, being able to image the sample and test the mechanical properties with an unprecedented resolution (Fig. 2.11). In the following sections, few relevant examples of the AFM capabilities in this field are reported.

4.1.1 Assessing the Mechanics of Microparticles for Drug Delivery

A perfect example of the AFM potentiality is represented by the recent work of Palomba et al. [83] that developed and characterized a new class of polymer micro/nano-particles for drug-delivery applications. It was previously proposed that the stiffness of the drugs carrier could influence significantly the macrophages uptake of the carrier itself and, hence, influence the effectiveness of the treatment. In particular, the cellular uptake, by bone marrow-derived monocytes, of particles with different shapes (circular, elliptical, and quadrangular) and with two typical sizes (1,000 and 2,000 nm) was characterized as a function of the particles stiffness. Discoidal particles were obtained in a multistep process via replica molding [55]. Different experimental techniques can provide the morphological characterization of micro-size particles. In particular, the authors employed confocal microscopy and transmission electron microscopy to have a fast characterization of a high number of samples. The elasticity of the polymer disks is the key parameter in this

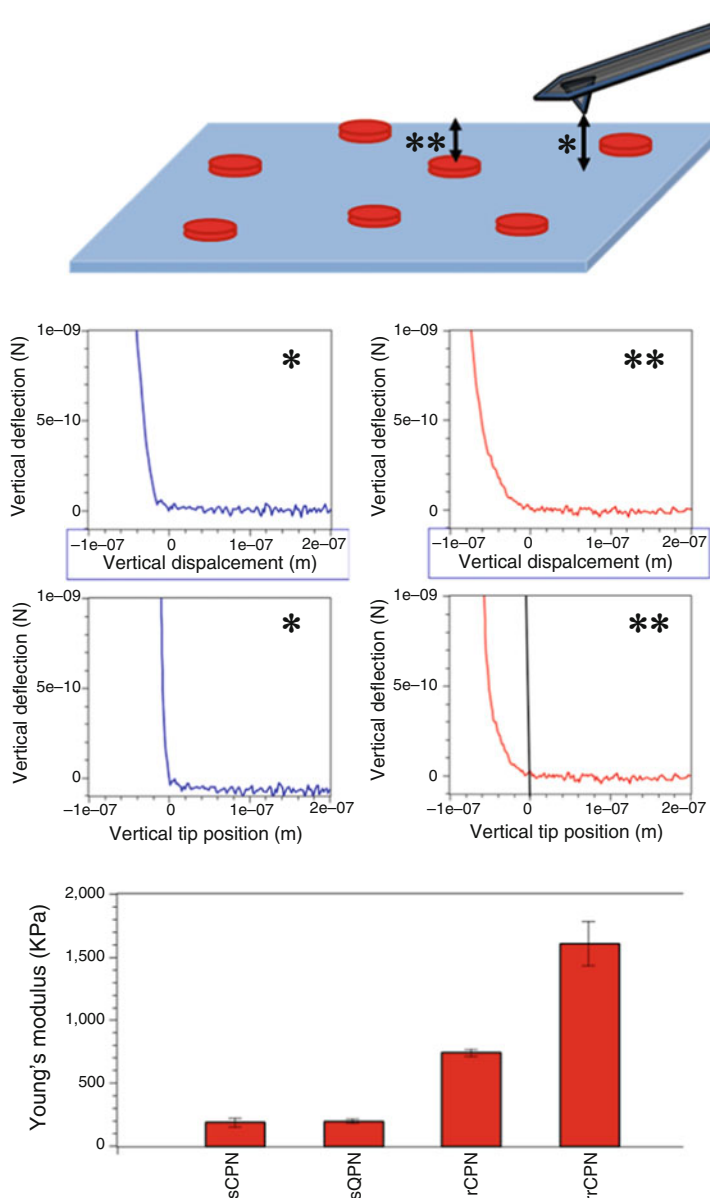


Fig. 2.11 A schematic representation of the experimental conditions is shown (top images). The soft disks, represented as red circular particles, are randomly distributed on the glass substrate. The sharp AFM tip can test the stiffness locally, and the analysis can be limited on the softer particles only. Two typical F-D curves and the correspondent F-I curves acquired on glass (*, left column) and on polymer disks (**, right column) are shown. A significant indentation is only present in **. The Young's moduli of CPN with three different composition (s, soft; r, rigid; and rr, very rigid) are shown in the bottom panel. The elasticity of soft square particle is also shown

investigation, and its experimental determination is fundamental, since the mechanical properties of the bulk polymer can be modified by the fabrication process and by the particle geometry itself. This characterization cannot be obtained using standard indentation methods that provide reproducible results only on extended samples and, generally, applying indentation forces that are not suitable for the study of a thin layer of soft material.

By using the AFM, the authors were able to identify the particles deposited on a standard glass slide, from the topographical reconstruction of the sample and to perform indentation experiments only on selected area (on the disk surface), applying a force load of 1 nN. All the analysis was performed in liquid environment, hence avoiding the stiffening effect induced by polymer dehydration. One of the main problems in the analysis of thin layers of soft materials lying on a rigid substrate is related to the influence of the stiffer substrate. In order to minimize the substrate contribution to Young's modulus determination, the authors applied small indentation depths, below the 10% of the particles thickness, also for the softer particles. The typical aspect of force vs. distance (F-D) curves obtained on soft, rigid, and overrigid substrates is shown in Fig. 2.11. F-D curves were corrected for the bending of the cantilever (36) to calculate the vertical tip position and to build force vs. indentation (F-I) curves (Fig. 2.11). Since the Hertz's model of contact mechanics is valid for spherical symmetry, the authors used the Bilodeau formula for pyramidal indenter [15], a generalization of the Hertz's model 4 that adapts it for square-shaped indenter putting $\rho = 0.7453tg\alpha$ and $\beta = 2$. F-I curves were thus fitted by using the following expression (Bilodeau's formula) 2.8,

$$F = 0.7453tg\alpha \frac{E}{1 - \nu^2} \delta^2 \quad (2.8)$$

where F is the force load, E is the Young's modulus, δ is the indentation depth, α is the face angle of the pyramid. Some manufacturer are not providing the angle α , but the angle measured at the corner edge, in this case, α can be deduced from trigonometric relations. Figure 2.11 shows an example of F-D curves acquired on the polymer disks and on the rigid substrate, and the correspondent F-I curves.

Palomba et al. demonstrated that the particle stiffness is not significantly affected by the particle shape, while changing the composition the stiffness can be reproducibly controlled (Fig. 2.11). The Young's moduli of circular (sCPN) and square (sQPN) particles with the same composition are shown in Fig. 2.11, as well as the elasticity of circular particles with a different composition (rCPN and rrCPN) are shown in figure (Fig. 2.11). For further details, also on other shape and composition particles, see [83]. The analysis performed by Palomba et al. [83] demonstrated particle stiffness can be tuned by varying the composition, in particular, softer disks are produced by increasing the PEG concentration. On the contrary, this work indicated that the geometry is just slightly affecting the mechanical properties of the particles. It was confirmed that, independently from the shape, softer particles interact less with macrophage, hence, they possess better biomimetic properties, being ideal candidates in drugs release applications.

4.2 Mechanical Properties of Porous Materials for Tissue Engineering

In the last decade, several applications focused on the use of soft porous and fibrous materials as cell scaffold for tissue regeneration [6, 63, 86, 109]. These materials are a valid 3D model of the extracellular matrix. They have interesting mechanical properties in terms of elasticity and stability upon compression. Furthermore, the presence of large and interconnected empty spaces provides an optimal environment for the ingrowth of cells and tissue formation and for an efficient vascularization. A great attention must be put in the characterization of porous and fibrous 3D materials since their mechanical properties depend on the spatial scale that is considered. Welzel et al. [126] investigated the elastic modulus of porous materials for cell scaffold application prepared by freezing glycosaminoglycan–poly(ethylene glycol). In particular, they employed AFM-based nanoindentation, by using a standard AFM tip as indenter. The AFM offers the possibility to test the stiffness of selected parts of the sample (Fig. 2.12). Starting from thin slices of materials, Welzel et al. concentrated the investigation on the scaffold wall, obtaining the elastic modulus of the material and avoiding the softening effect induced by porosity. Comparing these results with that obtained on the bulk hydrogel, they found that the process of pore formation induced by cryo-concentration significantly increased the elastic modulus of the material. This result was expected but still not confirmed experimentally.

Offeddu et al. [78] show a very explicative case by studying the multiscale mechanical properties of collagen scaffolds obtained through freeze-dried technique [78]. Freeze-drying is a consolidated technique for the fabrication of 3D polymer scaffold with controlled pore size and wall thickness [77, 87]. Previous work demonstrated that the scaffold pore size influence significantly adhesion, growth, and phenotype of cells [95, 124, 132].

Similarly, it has also been shown that Young's modulus of the bulk porous material increase with the concentration of collagen, i.e., with the concentration of solid in the material [47]. For tissue engineering and regeneration, the global stiffness of the porous 3D scaffold is essential, since this has to adapt to the stiffness of the host tissue/organ. On the other hand, the single cells are feeling the local stiffness, interacting with a limited portion of a pore wall with an area in the order of hundreds of μm^2 . The bulk stiffness is measured by standard indentation methods, by using large spherical indenter with a diameter of 1.2 mm and applying indentation of 0.5 mm (Fig. 2.12 c). The bulk stiffness increased quadratically by increasing the concentration of collagen, and this is due to the presence of a higher number of pores and an increased amount of material forming the walls (i.e., thicker walls). An interesting AFM approach was employed to evaluate the elasticity of single membrane of the material that forms the pore.

The analysis indicates that the mechanical properties of the single scaffold membranes, i.e., the mechanical environment felt by single cells seeded on this kind of scaffold, is the same, independently from collagen concentration (Fig. 2.12 f), on the contrary, the global stiffness of the device is influenced by

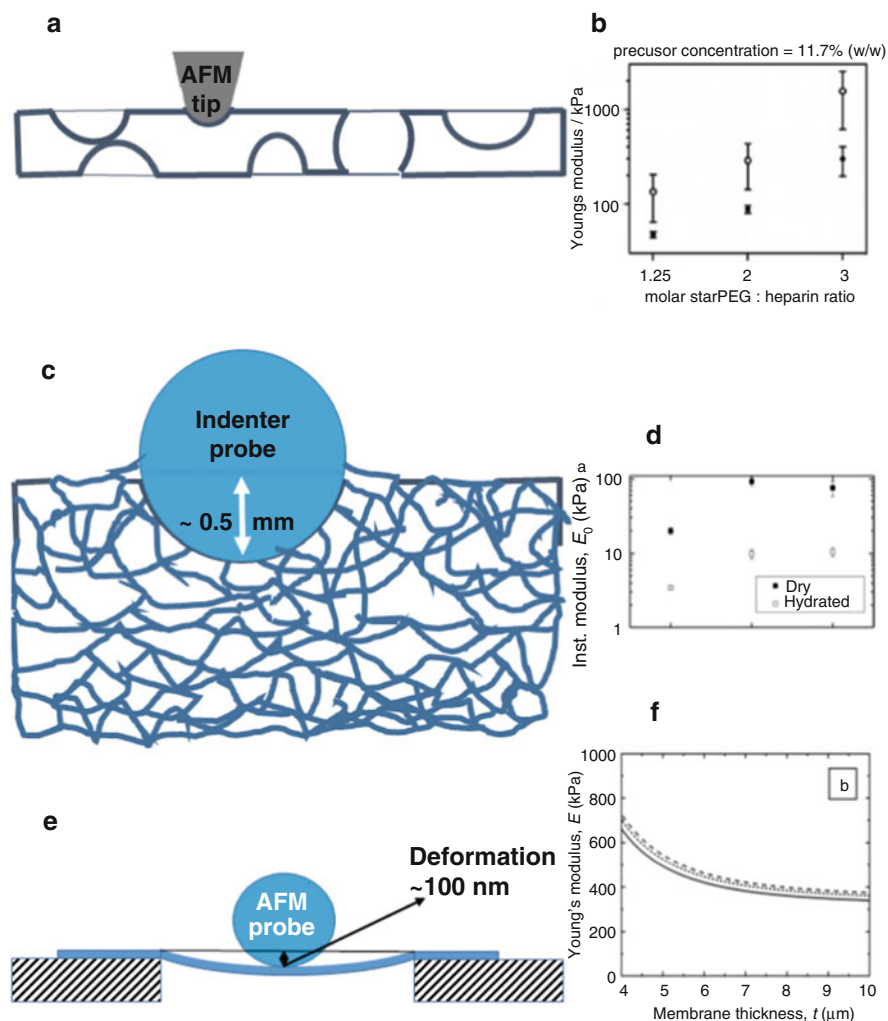


Fig. 2.12 (a) Schematic representation of the experimental design. A thin slice of porous material is prepared and deposited on a rigid substrate. By using a standard AFM tip only the walls are tested. The analysis is performed on hydrated samples. (b) Instantaneous Young's moduli calculated for the cryogel struts (open circles) and the corresponding bulk hydrogels (closed circles), modified from Welzel et al. [126]. The material that forms the wall of freezing-induced pores is stiffer than the bulk material. The stiffness is also dependent on the composition. Two approaches are proposed by Offeddu et al. [78], first, (c) large indentation with a standard indenter probe. The presence of the empty pores space decreases the stiffness of the bulk (d, modified from Offeddu et al. [78]). Dehydration is severely affecting the scaffold stiffness (d). The same kind of porous material is prepared differently for the AFM inspection. A thin slice is deposited on a copper grid with large pore (2.12 e). A microsize bead is pushed on the wall of a scaffold pore that stand above a grid pore. In this way not only the indentation but also a bending of the membrane of polymer is induce. The results derived from this experiment are shown in Fig. 2.12 f (modified from Offeddu et al. [78])

the concentration (Fig. 2.12 d), due to an increase of the scaffold wall thickness and this factor is important to adapt to the stiffness of the hosted organ.

Both papers here presented use standard AFM indentation methods, based on the acquisition of force-distance curves acquired in static mode (the AFM probe is not oscillating during the force-distance cycle), but the different experimental designs impose a different data treatment. Welzel et al. neglected the bending of the material and they applied the Bilodeau formula 2.8 for a pyramidal indenter, with α is the half-angle-to-face of the indenter (17.5° in this case).

On the contrary, Offeddu et al. tested the elasticity of relatively thin membranes that stand over the free space of a copper grid, hence, allowing membrane bending. In this case, the contribution of the deflection of the membrane must be considered, since it contributes, to define the correct elastic modulus of the membrane. A different model was chose to fit the experimental data, in particular, the author applied the model previously developed by Scott et al. [107], here shown in 2.9.

$$E = E_{\text{penetration}} + E_{\text{deflection}} = \sqrt[3]{\frac{9P^2(1-\nu^2)^2}{16rh^3}} + \frac{3Pa^2(1-\nu^2)}{4\phi t^3} \quad (2.9)$$

where E is the Young's modulus of the material, P is the measured load, t the thickness of the membrane, and ν the Poisson's ratio of the material.

Some of the primary results are summarized in Fig. 2.12. In particular, the discrepancy in the elastic moduli registered on collagen scaffolds (Fig. 2.12 d, f) is due to the different scale of analysis. The E of bulk porous materials results smaller, less than 10 KPa when hydrated, indicating that the scaffold is a very soft material, suitable for soft tissue regeneration purpose, while the local elasticity is more than one order of magnitude higher (Fig. 2.12). The interplay between local and bulk elasticity is an important parameter that can be controlled to create a good biomimetic environment.

4.3 Noncontact Mechanical Analysis

A complementary nondestructive, non-invasive and label free approach for the mechanical characterization of biomaterials is provided by Brillouin spectroscopy, which discovered in recent years new breakthroughs in instrumentation (see paragraph 2.2.1), enabling new applications areas [19, 73].

In the following we will focus our attention on two different application methods of the technique, exploiting BLS either to characterize the visco-elatic properties of homogeneous natural and/or artificial bio-materials, or as an imaging tool able to resolve bio-mechanical modulations with sub-cellular spatial resolution.

4.3.1 Brillouin Spectroscopy of Biomaterials

The first Brillouin applications for the bio-materials investigation appeared in the seventies, characterizing the elastic moduli of collagen, muscle [31, 46], eye

tissues such as crystalline lens and cornea [91, 121], aligned multilamella lipid samples [59] and DNA fibres [66].

After these pioneering studies which, for the first time, demonstrated the ability of the technique, many other studies have been addressed over time, analysing the link between morphology, composition, temperature and pressure conditions and elastic properties in bio-materials.

As a first relevant example, BLS has been successfully applied to study biomimetic materials with tunable elastic parameters, helping to design innovative bio-inspired samples aimed at mimicking different tissues stiffness. In brief, a platform based on chemically modified hydrogels from denaturalized collagen (GelMA) was adopted obtaining a photo-crosslinkable polymeric system responsive to UV exposure [76, 129]. Brillouin spectroscopy demonstrated its ability to follow the viscoelastic modulation obtained changing the concentration of the covalently crosslinked hydrogels. In fact, a good positive correlation has been found between the Brillouin frequency shift and the storage/loss modulus measured by shear-rheology in the different samples [73] (Fig. 2.12).

Moreover, BLS resulted to be effective also to characterize the interaction of biomembranes models with molecules potentially able to modify the lipid phase transitions. To analyze at molecular level the role of sugar in the protective action during drying or freezing in model membranes, the multi-lamellar lipidic assemblies has been studied as a function of temperature by infrared, Raman and Brillouin spectroscopies [96]. The collective dynamics measured by BLS evidenced the different temperature dependence measured in hydrated and dry samples with and without trehalose crossing the gel to liquid-crystalline phase transitions. The comparison with Raman and infrared spectroscopies links the collective dynamics with the molecular interactions.

BLS has been widely used also for natural biomaterials characterization, as occurred for example in the case of spider silk. This system has unique mechanical characteristics and analysing by BLS the different directions along the fibers, five independent elastic constants were determined [58]. Moreover, an intriguing and complex scenario of its dynamical properties has been revealed discovering the presence of a hypersonic phononic band-gap and a negatively dispersive region. The origin of these peculiar dynamical properties has been attributed to the link between non linearity in the mechanical response and the multilevel structural organization of the silk fiber [105]. These studies can give an important insight for the design of new bio-engineered meta-materials.

Recently, Brillouin studies has been performed using the innovative scattering geometry reported in Fig. 2.13 [34, 35, 85] which deserve a separate description. The experimental configuration has been used for the characterization of elastin and collagen, the principal fibrous, load-bearing components of the extracellular matrix.

Being the main components of bones, muscles and tendons the Extra Cellular Matrix (ECM) has a key role in the body functionality. It has a multidomain structure which starting from the nano-and micro-meter length scale develops on the macroscopic scale. The sophisticated ECM architecture and its role in the transmission of

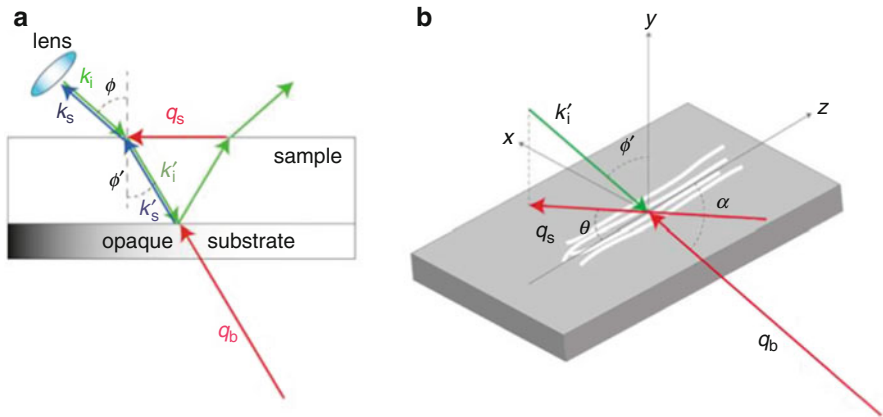


Fig. 2.13 Schematic diagram of the BLS geometry using the protein fibers in contact with the surface of a reflective silicon substrate. (Reprinted with permission from [85])

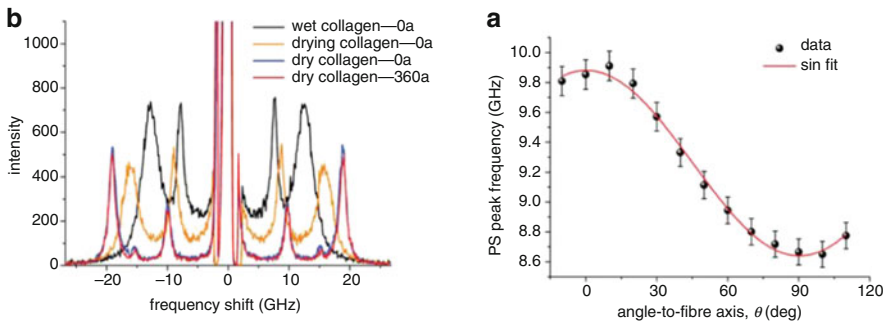


Fig. 2.14 Left panel: BLS spectra at different angle θ , in degrees, respect to the fibre axis. The letters ‘a’ and ‘r’ refer respectively to axial and radial directions of the exchanged wavevector respect to the fibre axis. Right panel: Plot of the frequency of the PS peak in a dry collagen fibre as a function of angle θ to the fibre axis. Data are fitted to a sinusoidal function. (Reprinted with permission from [85])

the mechanical stimuli to the cells attracted enduring interest of the scientific community [125].

In the new proposed experimental configuration the fibres, mainly aligned along a given direction, are in contact with a reflective silicon substrate which acts as a mirror for the incoming laser beam. In this way, two scattering processes occurs. The former is due to the usual interaction of the phonons with the incoming laser beam, giving rise to the so called bulk peak. The latter is due to the scattering of the phonons with the beam virtually generated by the reflective substrate. This second process probes the phonons travelling parallel to the substrate surface generating a second peak in the Brillouin spectrum (parallel-to-surface, PS mode) see Fig. 2.14a. Thanks to this configuration, it is possible (i) to evaluate the fibres elastic moduli

regardless of the accurate estimation of the refractive index of the medium and (ii) rotating the sample, to reveal both longitudinal and transverse acoustic waves travelling at different angles along the fiber axis assuring the complete acoustic characterization of the system. As suggested in the earliest studies [31], the fibres can be modelled as hexagonal symmetric elastic solid. The frequency position of the PS Brillouin peak measured at different angles changes as shown in Fig. 2.14b, and, from this modulation, four of the five elastic constants that characterize its elasticity tensor can be obtained. Imposing the relation between the elastic moduli, the axial and transverse Young's, the shear and the bulk moduli of the fibres has been evaluated finding 10.2, 8.3, 3.2 and 10.9 GPa, and 6.1, 5.3, 1.9 and 8 GPa for dehydrated type I collagen and elastin, respectively. These values, especially in the elastin case, are much higher than those obtained by the low frequency investigations [20, 97].

Moreover, the well known difference [20, 43] of two orders of magnitude between the elastin and collagen fibres elastic modulus is no more present analysing the system in the GHz frequency range. As already noted by Cusack and Miller in their pioneering work [31], the data disclose the presence of relaxation process with a characteristic time much slower than the time scale probed by BLS. In fact, this behaviour can be explain, as previously introduced in the paragraph 2.2.3, in term of the visco-elastic nature of the materials and to the different elastic moduli probed by the techniques.

4.3.2 Bio-Mechanical BLS Imaging

In the analysis of spatially heterogeneous materials such as cells and tissues, the evaluation of mechanical properties has to be addressed passing from single point analysis to a scanning mode approach. The increased spatial resolution obtained coupling Brillouin spectroscopy with microscopy, the drastic reduction in acquisition time and the increase of the experimental contrast obtained by the implementation of the spectrometers, as reported in paragraph 2.2.2, paved the way to new application possibilities.

BLS spectroscopy has been recently used to map the elastic heterogeneity in tissues [1, 4] recognising distinct anatomical structures living organisms [104]. The first studies of the in-situ 3D mechanical mapping of a mouse eye [98] further developed achieving the ability to obtain the in vivo Brillouin map of the full human eye in 2012 [100] anticipate the potential impact in ophthalmology [54, 131]. The modifications of the tissues elasticity in human pre-cancerous epithelial tissue studied in Barrett's oesophagus biopsies [84] or in Sinclair miniature swine, an accepted animal model for the human melanoma [71], highlighted the possibility to use BLS for the cancer diagnostics or therapeutics.

A correlative Brillouin and Raman approach has been also used to study the hippocampal part of the brain of transgenic mouse affected by amyloidopathy [68].

Both the experimental techniques proved to successfully differentiate the amyloid plaques and the healthy tissue highlighting the strict relation between the modifications of mechanical properties and chemical composition with the development of this pathology. In fact, the Brillouin imaging of the brain reported in

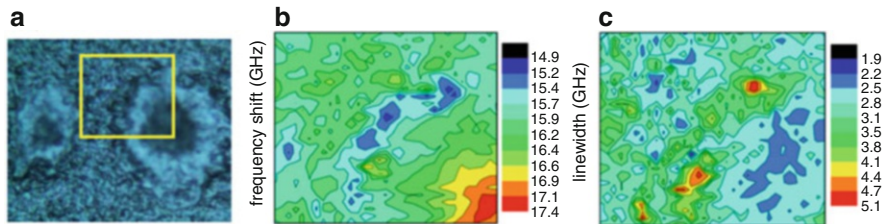


Fig. 2.15 (a) Image of the hippocampal section of a transgenic mouse brain containing two amyloid plaques. (Yellow box denotes a $50 \times 43 \mu\text{m}^2$ area where a Brillouin map was acquired using a $1.5 \mu\text{m}$ step-size. (b) Maps of the frequency shift and (c) linewidth of the Brillouin peak. (Reprinted from [68])

Fig. 2.15 shows an increase in the Brillouin shift investigating the core of the plaque. This region is more rigid than the surrounding tissue: the increase of about 10% found in the Brillouin frequency corresponds, neglecting density and refractive index changes, to an increase of about 20% in the longitudinal elastic modulus. The comparison with the Raman maps obtained investigating the same tissue region, shows that chemical modifications correspond to mechanical changes. In particular, the amyloid plaques structure presents a rigid core rich of protein in β -sheet conformation surrounded by a softer region rich in lipid and proteins in other conformational structures. In fact, it has been already observed that different types of protein aggregates correspond to different rigidity in particular random coil structures are softer than α -helix, which in turn are softer than aggregates in β -sheet conformation [88].

An other interesting aspect to underline in this study is the clear relationship between the width, $\Gamma_b(\Omega_b)$, and the frequency, Ω_b , of the Brillouin peak as showed in Fig. 2.15. Leaving the core of the plaque, the Brillouin frequency shift decreases, reaching its minimum value in the region of the lipid ring while the opposite behaviour has been found for the width of the Brillouin peak. The reduction of Ω_b , related with the real part of the longitudinal elastic modulus

$$M'(\Omega_b) = \rho\Omega_b^2/q^2$$

(where ρ is the density and q the exchanged wavevector, defined in Eq. 2.5), correlates quite strictly with an increase of $\Gamma_b(\Omega_b)$, related with $M''(\Omega_b)$, the imaginary part of the longitudinal elastic modulus, and with $\eta_L(\Omega_b)$ the longitudinal apparent viscosity as

$$\eta_L(\Omega_b) = M''(\Omega_b)/\omega = \rho\Gamma_b/q^2$$

A part from the key role played by the different chemical compositions in the modulation of the elastic properties, this experimental result could hide a possible viscoelastic origin. In fact, in the framework of the viscoelastic description in presence of relaxation phenomena, the direct correlation between the real and the

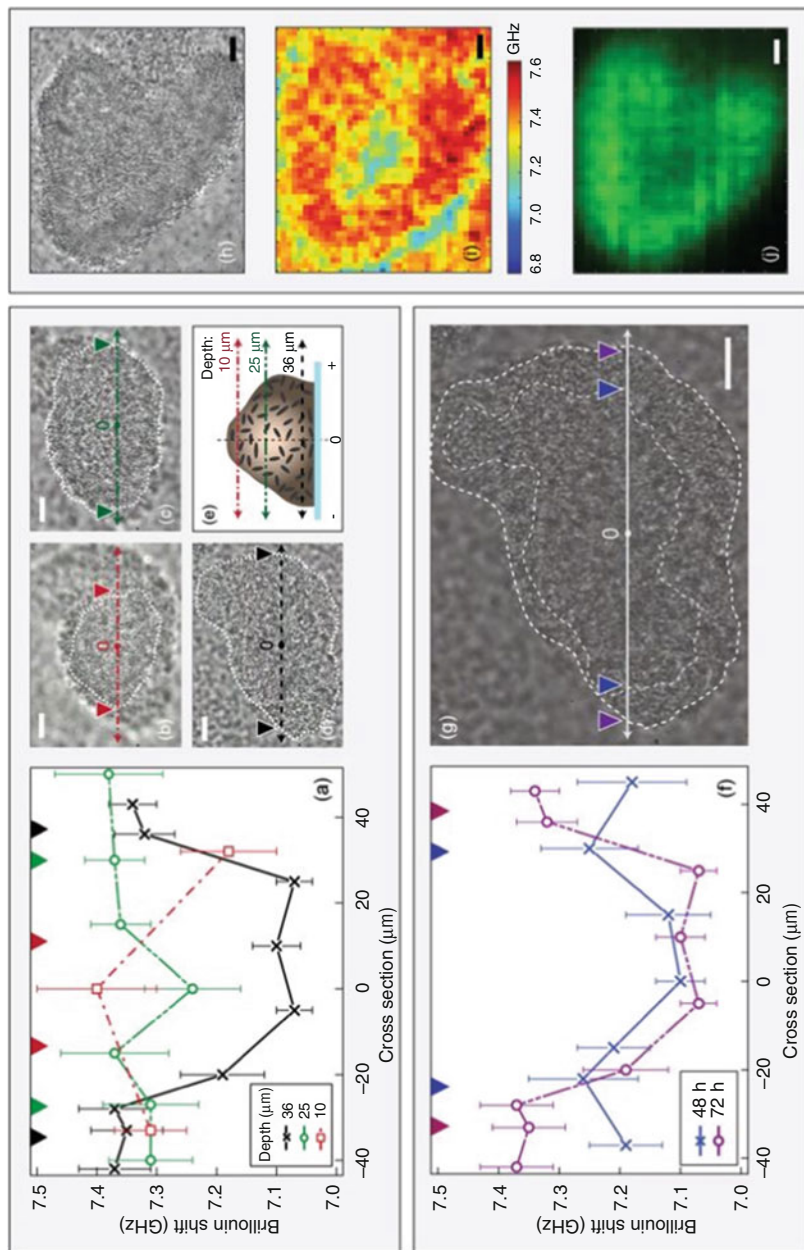


Fig. 2.16 (continued)

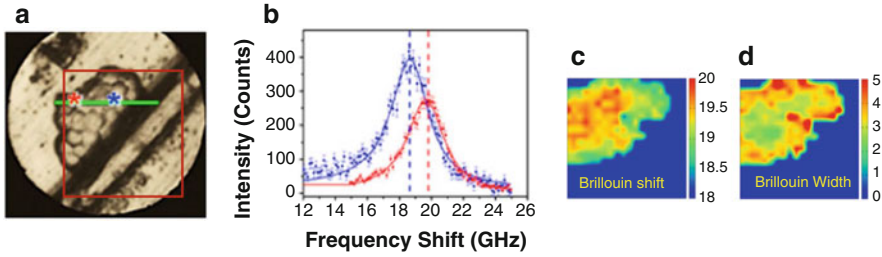


Fig. 2.17 (a) Optical micrograph of a *Candida albicans* biofilm. The red box denotes the $20 \times 20 \mu\text{m}^2$ area where Brillouin raster-scan maps are performed with $1 \mu\text{m}$ step-size. (Reprinted from [69, 103]). (b) Brillouin spectra (dots) measured in the points indicated by asterisks in (a). The full lines are the fitting curves obtained by a damped harmonic oscillation, DHO, model $I(\omega) = I_0 \Gamma_B \Omega_B^2 / \pi \left((\omega^2 - \Omega_B^2)^2 + (\Gamma_B \omega)^2 \right)$. (Reprinted from [69]). (c) and (d) Brillouin maps respectively based on the characteristic frequency Ω_b (GHz) and linewidth Γ (GHz) of the Brillouin peak. (Reprinted from [103])

imaginary part of the elastic modulus is expected if the frequency probed by the technique is lower than the characteristic frequency of the structural relaxation time. Otherwise the opposite behaviour is expected (see Fig. 2.10).

Besides the bio-mechanical mapping of tissues, applications at smaller length scales are recently performed, analysing for example biofilms as complex cells aggregates [53, 103]. Biofilms, the so called “city of microbes” is composed by microbial cells able to reach high level of resistance to antibiotics, anti-fungal drugs and extreme conditions. This ability is in part related to the solid surfaces surrounding the cells consisting of eso-polysaccharides (EPS) a cross-linked polymeric structure produced by the cells themselves. The mechanical characteristics of the biofilm appear of key importance for the understanding of its resistance ability or the mechanisms governing its lifecycle, which includes cells adhesion on surfaces, growth and maturation of the colony and dispersion of new cells to build a new biofilm.

Being a spectroscopic technique, Brillouin spectroscopy is able to provide a mechanical characterization not limited to the surface, allowing the detection of



Fig. 2.16 Brillouin study of *Pseudomonas aeruginosa* biofilms colonies. (a) Frequency shift of the Brillouin peak measured along cross-sections of a single colony (thickness $38 \mu\text{m}$, taken at 72 h post inoculation), depths are indicated. The coloured triangles on the top border denotes the colony boundaries at each depth corresponding to panels from (b) to (d) where the wide field images of the studied colony taken at different depths of 10, 25 and $36 \mu\text{m}$ are reported. The white dashed lines define the boundaries of the colony at each depth. (e) Schematic picture of the cross-sections. (f) Time evolution of the Brillouin shifts measured along the cross-section of a single colony at 48 and 72 h post inoculation. (g) Wide field image of the same colony, taken at 48 and 72 h post inoculation. (h) Wide field, (i) Brillouin, and (j) Fluorescence images of a different colony imaged 100 h post inoculation taken at a depth of $15 \mu\text{m}$ inside a $35\text{-}\mu\text{m}$ thick biofilm. Scale bars: $10 \mu\text{m}$. (Reprinted from [53])

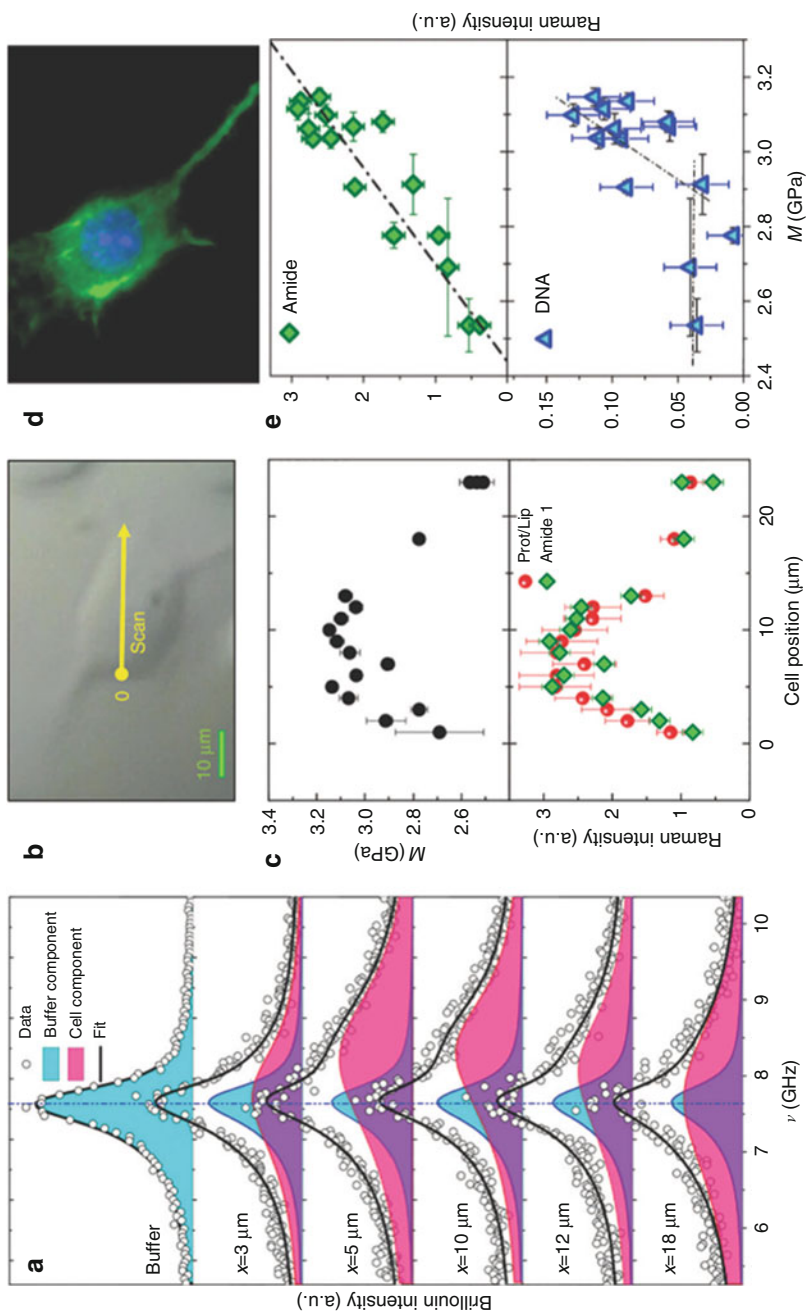


Fig. 2.18 (continued)

the bulk mechanical properties, well below the EPS matrix or the first cells layer of the biofilm. This ability is a clear advantage with respect to other techniques, like for example atomic force microscopy, able to reach higher spatial resolution, but mainly on the sample surface. Changing the position of the laser beam focus, different depths into the intact and live colony can be analyzed. The data [53] show a modification in mechanical properties at different times post inoculation showing how the mechanical properties can be used as marker to characterize the life-cycle of the colony (see Fig. 2.16).

The study of biofilms has been recently approached also by a correlative Brillouin and Raman spectroscopy [69, 103]. The Brillouin image of a dry sample of *Candida albicans* biofilm grown on a metallic substrate is reported in Fig. 2.17.

Using the Raman peaks as spectroscopic markers of modification in the cell status and/or in the biofilm composition, the study evidences the potential presence of still alive *Candida* cells in a dried sample maintained at room temperature for 1 week before the analysis. The existence of a softer region revealed by Brillouin scattering correlated with a region where the Raman signals drastically change revealing also the presence of residual water. These results confirm the microbiological properties of biofilms, which are able to preserve water and to protect cells acting as a defence structure against adverse external agents.

The Brillouin imaging even reached the sub-micrometric spatial resolution achieving the possibility to analyse mechanical modulations of subcellular compartments in living cells. The technique holds the promise to unveil new aspects of the cell biology since it is able to perform in situ analysis without the use of any fixation procedure and the presence of the buffer does not hamper the signal detection. The clear discrimination of the sub-cellular elastic heterogeneities are obtained in several cases [2, 36, 70, 72, 102], together with the evidences of elastic properties modifications in the cells after oncogenic transfection [70], after osmotic shock [102], after the exposure to latrunculin-A, a toxin that prevents polymerisation of actin filament [2]. Recently BLS has been



Fig. 2.18 (a) Brillouin spectra and their deconvolution into cell and buffer components. The fit was performed by considering a fixed shape of the buffer contribution (sound velocity and kinematic viscosity of the corresponding DHO function). Leaving these parameters as free, or even adding a further DHO function, would not lead to an increase in R^2 . (b) Cell image. The yellow point is the initial investigated point for the illustrated measurements. The straight arrow along the cell shows the direction in which the measurements were performed. (c) Upper panel Longitudinal elastic modulus M' as a function of the position. Lower panel relative variation of the protein concentration as obtained by the area of the amide I Raman peak and by the deconvolution of the carbon – hydrogen (CH) stretching vibrational mode. (d) Fluorescence microscopy image of NIH/3 T3 cell seeded onto glass cover slips. The average value of the nuclei size is $(14 \pm 2) \mu\text{m}$, in good agreement with the Raman spectroscopic signatures of the cell nucleus. (e) Raman peak intensities of the protein estimated by the intensity of the amide I peak and the DNA vs the longitudinal elastic modulus. (Reprinted from [70])

also used to analyse the roles for mechanotransduction in embryonic development [89]. A recent correlative Raman and Brillouin investigation has been performed analyzing single living fibroblasts cells [70]. The Brillouin line shape visibly changes probing different sub-cellular compartments, see Fig. 2.18a, highlighting the technique sensitivity to the local mechanical properties. In these measurements, the presence of the buffer inside the scattering volume is revealed analysing the shape of the Brillouin peak, which appears composed by a superposition of two contributions. The former, which changes its frequency position due to the signal of the cell, and the latter which instead remains at the same frequency changing only its intensity due to the buffer. Using an innovative fitting procedure the two components has been easily separated thereby obtaining the local longitudinal elastic modulus and viscosity. Both the obtained viscoelastic parameters appear modified analysing different positions inside the cell. The correlative analysis lets to link the mechanical evolution found by BLS measurements with the corresponding biochemical composition obtained by Raman spectroscopy. The data highlights the link between the protein concentration and the cell elasticity confirming the key role of protein structures in conferring rigidity to the cells.

5 Conclusions and Future Perspective

Measuring and mapping mechanical properties of biomimetic materials with a resolution below 1 μm is one of the key technological challenges in characterization tools for tissue engineering and regenerative medicine. Nowadays, the most effective approaches are based either on atomic force microscopy or exploiting Brillouin spectroscopy. The former has the highest resolution and a quite robust literature background, but it requires to enter in contact with the sample to probe its elasticity, thus inducing several issues in the wide application of AFM in every day practice and translation to medicine. On the other side, BLS is a very promising remote elasticity mapping technique, but several technical limitations have still to be overcome, among which the speed and the resolution.

Moreover, besides all the discussed experimental tricky points still present in AFM and BLS, a crucial theoretical and phenomenological question is also open. In fact, AFM and BLS not only exploit a different approach, but they intrinsically address different dynamical regions: the AFM probes the mechanical properties in the quasistatic regime (below 1–10 kHz, but often few Hz), while BLS attain the high frequency region (in the range of GHz). Some tentatives have already been done to recapitulate the two domains [35, 101, 102], also proposing the existence of a scaling law (see Fig. 2.10). Nevertheless, this experimental observation still deserves an in-depth phenomenological and theoretical investigation, requiring to combine the two approaches in order to assess the underlying theoretical framework. In addition, this consideration also points out that a multi-scale approach is an essential requirement to have the complete characterization of any viscoelastic material [8, 97, 114]. This is particularly important, in

the characterization of biomimetic materials designed to interface with cells or tissues, whose dynamical processes span over several decades in length and time. The combined use of experimental techniques which in complementary way cover the system dynamics is an important requirement to provide novel insights in their design and to modulate the structure-function relationships.

References

1. Akilbekova D, Ogay V, Yakupov T, Sarsenova M, Umbayev B, Nurakhmetov A, Tazhin K, Yakovlev VV, Utegulov ZN (2018) Brillouin spectroscopy and radiography for assessment of viscoelastic and regenerative properties of mammalian bones. *J Biomed Opt* 23(9):097004
2. Antonacci G, Braakman S (2016) Biomechanics of subcellular structures by non-invasive Brillouin microscopy. *Sci Rep* 6:37217. <https://doi.org/10.1038/srep37217>
3. Antonacci G, Foreman MR, Paterson C, Török P (2013) Spectral broadening in Brillouin imaging. *Appl Phys Lett* 103(22):221105. <https://doi.org/10.1063/1.4836477>. <http://adsabs.harvard.edu/abs/2013ApPhL.103v1105A>
4. Antonacci G, Pedrighi RM, Kondiboyina A, Mehta VV, De Silva R, Paterson C, Krams R, Török P (2015) Quantification of plaque stiffness by Brillouin microscopy in experimental thin cap fibroatheroma. *J R Soc Interface* 12(112):20150843
5. Antonacci G, De Panfilis S, Di Domenico G, DelRe E, Ruocco G (2016) Breaking the contrast limit in single-pass fabry-pérot spectrometers. *Phys Rev Appl* 6(5):054020. <https://doi.org/10.1103/PhysRevApplied.6.054020>. <http://adsabs.harvard.edu/abs/2016PhRvP..6e4020A>
6. Barenghi R, Beke S, Romano I, Gavazzo P, Farkas B, Vassalli M, Brandi F, Scaglione S (2014) Elastin-coated biodegradable photopolymer scaffolds for tissue engineering applications. *Biomed Res Int* 2014:624645
7. Bavi N, Nikolaev YA, Bavi O, Ridone P, Martinac AD, Nakayama Y, Cox CD, Martinac B (2017) Principles of mechanosensing at the membrane interface. In: Epanand R., Ruyschaert JM. (eds) *The Biophysics of Cell Membranes*. Springer Series in Biophysics, vol 19. Singapore: Springer
8. Bechtle S, Ang S, Schneider G (2010) On the mechanical properties of hierarchically structured biological materials. *Universitätsbibliothek der Technischen Universität Hamburg-Harburg, Hamburg*. <https://books.google.it/books?id=nW5QuwEACAAJ>
9. Benassi P, Caponi S, Eramo R, Fontana A, Giugni A, Nardone M, Sampoli M, Viliani G (2005) Sound attenuation in a unexplored frequency region: Brillouin ultraviolet light scattering measurements in v -si o_2 . *Phys Rev B* 71(17):172201. <https://doi.org/10.1103/PhysRevB.71.172201>. <http://adsabs.harvard.edu/abs/2005PhRvB.71q2201B>
10. Berne BJ, Pecora R (1977) *Dynamic Light Scattering with Applications to Chemistry, Biology, and Physics*. Courier Corporation, 54(10):A430 <https://doi.org/10.1021/ed054pA430.1>
11. Bettinger CJ, Langer R, Borenstein JT (2009) Engineering substrate topography at the micro- and nanoscale to control cell function. *Angew Chem Int Ed Engl* 48:5406–5415. <https://doi.org/10.1002/anie.200805179>
12. Betzig E, Trautman J, Harris T, Weiner J, Kostelak R (1991) Breaking the diffraction barrier: optical microscopy on a nanometric scale. *Science* 251(5000):1468–1470
13. Bhushan B (ed) (2010) *Scanning probe microscopy in nanoscience and nanotechnology*, vol 2. Springer, Berlin/Heidelberg
14. Bhushan B, Fuchs H (eds) (2008) *Applied scanning probe methods*, vol XIII. Springer, Berlin/Heidelberg
15. Bilodeau GG (1992) Regular pyramid punch problem. *J Appl Mech* 59:519. <https://doi.org/10.1115/1.2893754>

16. Binnig G, Rohrer H, Gerber C, Weibel E (1982) Surface studies by scanning tunneling microscopy. *Phys Rev Lett* 49(1):57
17. Binnig G, Quate CF, Gerber C (1986) Atomic force microscope. *Phys Rev Lett* 56:930–933. <https://doi.org/10.1103/PhysRevLett.56.930>
18. Boon J, Yip S (1991) *Molecular hydrodynamics*. Dover Publications, New York
19. Bottani CE, Fioretto D (2018) Brillouin scattering of phonons in complex materials. *Adv Phys: X* 3(1):1467281
20. Bracalello A, Santopietro V, Vassalli M, Marletta G, Del Gaudio R, Bochicchio B, Pepe A (2011) Design and production of a chimeric resilin-, elastin-, and collagen-like engineered polypeptide. *Biomacromolecules* 12:2957–2965. <https://doi.org/10.1021/bm2005388>
21. Brillouin L (1922) Diffusion of light and x-rays by a transparent homogeneous body. *Ann Phys* 17(2):88–122
22. Caponi S, Fontana A, Montagna M, Pilla O, Rossi F, Terki F, Woignier T (2003) Acoustic attenuation in silica porous systems. *J Non Cryst Solids* 322:29–34. [https://doi.org/10.1016/S0022-3093\(03\)00167-4](https://doi.org/10.1016/S0022-3093(03)00167-4). <http://adsabs.harvard.edu/abs/2003JNCS..322...29C>
23. Caponi S, Benassi P, Eramo R, Giugni A, Nardone M, Fontana A, Sampoli M, Terki F, Woignier T (2004a) Phonon attenuation in vitreous silica and silica porous systems. *Philos Mag* 84(13–16):1423–1431
24. Caponi S, Carini G, D'angelo G, Fontana A, Pilla O, Rossi F, Terki F, Tripodo G, Woignier T (2004b) Acoustic and thermal properties of silica aerogels and xerogels. *Phys Rev B* 70(21):214204
25. Cappella B, Dietler G (1999) Force-distance curves by atomic force microscopy. *Surf Sci* 34(1–3):1–3, 5–104
26. Carlotti G (2018) Elastic characterization of transparent and opaque films, multilayers and acoustic resonators by surface Brillouin scattering: a review. *Appl Sci* 8(1):124
27. Cavalleri O, Natale C, Stroppolo ME, Relini A, Cosulich E, Thea S, Novi M, Gliozzi A (2000) Azurin immobilisation on thiol covered au(111). *Phys Chem Chem Phys* 2:4630–4635
28. Chen C, Bang S, Cho Y, Lee S, Lee I, Zhang S, Noh I (2016) Research trends in biomimetic medical materials for tissue engineering: 3d bioprinting, surface modification, nano/micro-technology and clinical aspects in tissue engineering of cartilage and bone. *Biomater Res* 20(1):1. <https://doi.org/10.1186/s40824-016-0057-3>
29. Chu B (1976) *Laser spectroscopy*. (Book reviews: dynamic light scattering. With applications to chemistry, biology, and physics). *Science* 194:1155–1156. <https://doi.org/10.1126/science.194.4270.1155>. <http://adsabs.harvard.edu/abs/1976Sci...194.1155B>
30. Comez L, Masciovecchio C, Monaco G, Fioretto D (2012) Progress in liquid and glass physics by Brillouin scattering spectroscopy. *Solid State Phys* 63:1–77. Elsevier
31. Cusack S, Miller A (1979) Determination of the elastic constants of collagen by Brillouin light scattering. *J Mol Biol* 135:39–51
32. Dil J (1982) Brillouin scattering in condensed matter. *Rep Prog Phys* 45(3):285
33. Dimitriadis EK, Horkay F, Maresca J, Kachar B, Chadwick RS (2002) Determination of elastic moduli of thin layers of soft material using the atomic force microscope. *Biophys J* 82(5):2798–2810. [https://doi.org/10.1016/s0006-3495\(02\)75620-8](https://doi.org/10.1016/s0006-3495(02)75620-8)
34. Edginton RS, Mattana S, Caponi S, Fioretto D, Green E, Winlove CP, Palombo F (2016) Preparation of extracellular matrix protein fibers for Brillouin spectroscopy. *J Vis Exp*. <https://doi.org/10.3791/54648>
35. Edginton RS, Green EM, Winlove CP, Fioretto D, Palombo F (2018) Dual scale biomechanics of extracellular matrix proteins probed by Brillouin scattering and quasistatic tensile testing. In: *Society of photo-optical instrumentation engineers (SPIE) conference series*, vol 10504, p 105040J. <https://doi.org/10.1117/12.2290183>. <http://adsabs.harvard.edu/abs/2018SPIE10504E..0JE>
36. Elsayad K, Werner S, Gallemi M, Kong J, Guajardo ERS, Zhang L, Jaillais Y, Greb T, Belkhadir Y (2016) Mapping the subcellular mechanical properties of live cells in tissues with fluorescence emission–Brillouin imaging. *Sci Signal* 9(435):rs5–rs5
37. Engler AJ, Sen S, Sweeney HL, Discher DE (2006) Matrix elasticity directs stem cell lineage specification. *Cell* 126(4):677–689

38. Fabry B, Maksym GN, Butler JP, Glogauer M, Navajas D, Fredberg JJ (2001) Scaling the microrheology of living cells. *Phys Rev Lett* 87:148102. <https://doi.org/10.1103/PhysRevLett.87.148102>
39. Ferrera D, Canale C, Marotta R, Mazzaro N, Gritti M, Mazzanti M, Capellari S, Cortelli P, Gasparini L (2014) Lamin b1 overexpression increases nuclear rigidity in autosomal dominant leukodystrophy fibroblasts. *FASEB J* 28(9):3906–3918. <https://doi.org/10.1096/fj.13-247635>
40. Fink M, Tanter M (2010) Multiwave imaging and super resolution. *Phys Today* 63(2):28–33. <https://doi.org/10.1063/1.3326986>
41. Fiore A, Zhang J, Shao P, Yun SH, Scarcelli G (2016) High-extinction virtually imaged phased array-based Brillouin spectroscopy of turbid biological media. *Appl Phys Lett* 108:203701. <https://doi.org/10.1063/1.4948353>
42. Franz MO, Mallot HA (2000) Biomimetic robot navigation. *Robot Auton Syst* 30:133–153. [https://doi.org/10.1016/s0921-8890\(99\)00069-x](https://doi.org/10.1016/s0921-8890(99)00069-x)
43. Fung Y (1993) *Biomechanics: mechanical properties of living tissues*. Springer, New York
44. Gruber P (2008) The signs of life in architecture. *Bioinspir Biomim* 3:023001. <https://doi.org/10.1088/1748-3182/3/2/023001>
45. Hadden WJ, Young JL, Holle AW, McFetridge ML, Kim DY, Wijesinghe P, Taylor-Weiner H, Wen JH, Lee AR, Bieback K, Vo BN, Sampson DD, Kennedy BF, Spatz JP, Engler AJ, Choi YS (2017) Stem cell migration and mechanotransduction on linear stiffness gradient hydrogels. *Proc Natl Acad Sci U S A* 114:5647–5652. <https://doi.org/10.1073/pnas.1618239114>
46. Harley R, James D, Miller A, White JW (1977) Phonons and the elastic moduli of collagen and muscle. *Nature* 267:285–287
47. Harley BA, Leung JH, Silva ECCM, Gibson LJ (2007) Mechanical characterization of collagen-glycosaminoglycan scaffolds. *Acta Biomater* 3:463–474. <https://doi.org/10.1016/j.actbio.2006.12.009>
48. Hartmann U (1988) Magnetic force microscopy: some remarks from the micromagnetic point of view. *J Appl Phys* 64(3):1561–1564
49. Huang G, Li F, Zhao X, Ma Y, Li Y, Lin M, Jin G, Lu TJ, Genin GM, Xu F (2017) Functional and biomimetic materials for engineering of the three-dimensional cell microenvironment. *Chem Rev* 117(20):12764–12850. <https://doi.org/10.1021/acs.chemrev.7b00094>. PMID: 28991456
50. Hutter JL, Bechhoefer J (1993) Calibration of atomic-force microscope tips. *Rev Sci Instrum* 64(7):1868–1873. <https://doi.org/10.1063/1.1143970>
51. Ikada Y (2006) Challenges in tissue engineering. *J R Soc Interface* 3:589–601. <https://doi.org/10.1098/rsif.2006.0124>
52. Kapsali V (2013) 7 – Biomimetic approaches to the design of smart textiles for protection. In: Chapman R (ed) *Smart textiles for protection*. Wood-head Publishing series in textiles. Woodhead Publishing, Cambridge, UK, pp 214–226. <https://doi.org/10.1533/9780857097620.1.214>. <http://www.sciencedirect.com/science/article/pii/B9780857090560500078>
53. Karampatzakis A, Song CZ, Allsopp LP, Filloux A, Rice SA, Cohen Y, Wohland T, Török P (2017) Probing the internal micromechanical properties of *Pseudomonas aeruginosa* biofilms by Brillouin imaging. *NPJ Biofilms Microbiomes* 3:20. <https://doi.org/10.1038/s41522-017-0028-z>
54. Kennedy BF, Wijesinghe P, Sampson DD (2017) The emergence of optical elastography in biomedicine. *Nat Photonics* 11:215–221. <https://doi.org/10.1038/nphoton.2017.6>. <http://adsabs.harvard.edu/abs/2017NaPho..11..215K>
55. Key J, Palange AL, Gentile F, Aryal S, Stigliano C, Mascolo DD, Rosa ED, Cho M, Lee Y, Singh J, Decuzzi P (2015) Soft discoidal polymeric nanoconstructs resist macrophage uptake and enhance vascular targeting in tumors. *ACS Nano* 9(12):11628–11641. <https://doi.org/10.1021/acs.nano.5b04866>
56. Kim JH, Yoo JJ (2018) Current developments and future perspectives of tissue engineering and regenerative medicine. In: *Clinical regenerative medicine in urology*. Springer, Singapore

57. Klieber C, Hecksher T, Pezeril T, Torchinsky DH, Dyre JC, Nelson KA (2013) Mechanical spectra of glass-forming liquids. II. Gigahertz-frequency longitudinal and shear acoustic dynamics in glycerol and dc704 studied by time-domain Brillouin scattering. *J Chem Phys* 138:12A544. <https://doi.org/10.1063/1.4789948>
58. Koski KJ, Akhnenblit P, McKiernan K, Yarger JL (2013) Non-invasive determination of the complete elastic moduli of spider silks. *Nat Mater* 12:262–267. <https://doi.org/10.1038/nmat3549>
59. Lepesant JP, Powers L, Pershan PS (1978) Brillouin light scattering measurement of the elastic properties of aligned multilamella lipid samples. *Proc Natl Acad Sci U S A* 75:1792–1795
60. Lim C, Zhou E, Quek S (2006) Mechanical models for living cells – a review. *J Biomech* 39(2):195–216. <https://doi.org/10.1016/j.jbiomech.2004.12.008>
61. Lin DC, Dimitriadis EK, Horkay F (2007) Robust strategies for automated AFM force curve analysis – II: adhesion-influenced indentation of soft, elastic materials. *J Biomech Eng* 129(6):904. <https://doi.org/10.1115/1.2800826>
62. Lutolf MP, Gilbert PM, Blau HM (2009) Designing materials to direct stem-cell fate. *Nature* 462(7272):433
63. Ma PX (2008) Biomimetic materials for tissue engineering. *Adv Drug Deliv Rev* 60:184–198. <https://doi.org/10.1016/j.addr.2007.08.041>
64. Mandadapu KK, Govindjee S, Mofrad MRK (2008) On the cytoskeleton and soft glassy rheology. *J Biomech* 41:1467–1478. <https://doi.org/10.1016/j.jbiomech.2008.02.014>
65. Mapelli L, Canale C, Pesci D, Averaimo S, Guizzardi F, Fortunati V, Falasca L, Piacentini M, Gliozzi A, Relini A, Mazzanti M, Jodice C (2012) Toxic effects of expanded ataxin-1 involve mechanical instability of the nuclear membrane. *Biochim Biophys Acta* 1822:906–917. <https://doi.org/10.1016/j.bbadis.2012.01.016>
66. Maret G, Oldenbourg R, Winterling G, Dransfeld K, Rupprecht A (1979) Velocity of high frequency sound waves in oriented DNA fibres and films determined by Brillouin scattering. *Colloid Polym Sci* 257(10):1017–1020
67. Masciovecchio C, Baldi G, Caponi S, Comez L, Di Fonzo S, Fioretto D, Fontana A, Gessini A, Santucci S, Sette F et al (2006) Evidence for a crossover in the frequency dependence of the acoustic attenuation in vitreous silica. *Phys Rev Lett* 97(3):035501
68. Mattana S, Caponi S, Tamagnini F, Fioretto D, Palombo F (2017a) Viscoelasticity of amyloid plaques in transgenic mouse brain studied by Brillouin microspectroscopy and correlative Raman analysis. *J Innov Opt Health Sci* 10:1742001. <https://doi.org/10.1142/S1793545817420019>
69. Mattana S, Cardinali MA, Caponi S, Pierantoni DC, Corte L, Roscini L, Cardinali G, Fioretto D (2017b) High-contrast Brillouin and Raman micro-spectroscopy for simultaneous mechanical and chemical investigation of microbial biofilms. *Biophys Chem* 229:123–129
70. Mattana S, Mattarelli M, Urbanelli L, Sagini K, Emiliani C, Dalla Serra M, Fioretto D, Caponi S (2018) Non-contact mechanical and chemical analysis of single living cells by micro-spectroscopic techniques. *Light: Sci Appl* 7(2):17139
71. Meng Z, Traverso AJ, Yakovlev VV (2014) Background clean-up in Brillouin micro-spectroscopy of scattering medium. *Opt Express* 22:5410–5415. <https://doi.org/10.1364/OE.22.005410>
72. Meng Z, Bustamante Lopez SC, Meissner KE, Yakovlev VV (2016a) Subcellular measurements of mechanical and chemical properties using dual Raman-Brillouin microspectroscopy. *J Biophotonics* 9:201–207. <https://doi.org/10.1002/jbio.201500163>
73. Meng Z, Traverso AJ, Ballmann CW, Troyanova-Wood MA, Yakovlev VV (2016b) Seeing cells in a new light: a renaissance of Brillouin spectroscopy. *Adv Opt Photon* 8(2):300–327
74. Monaco G, Caponi S, di Leonardo R, Fioretto D, Ruocco G (2000) Intramolecular origin of the fast relaxations observed in the Brillouin light scattering spectra of molecular glass formers. *Phys Rev E* 62:R7595–R7598. <https://doi.org/10.1103/PhysRevE.62.R7595>. <http://adsabs.harvard.edu/abs/2000PhRvE..62.7595M>

75. Murphy SV, Atala A (2013) Organ engineering—combining stem cells, biomaterials, and bioreactors to produce bioengineered organs for transplantation. *BioEssays* 35:163–172. <https://doi.org/10.1002/bies.201200062>
76. Nichol JW, Koshy ST, Bae H, Hwang CM, Yamanlar S, Khademhosseini A (2010) Cellladen microengineered gelatin methacrylate hydrogels. *Biomaterials* 31(21):5536–5544
77. O'Brien FJ, Harley BA, Yannas IV, Gibson L (2004) Influence of freezing rate on pore structure in freeze-dried collagen-gag scaffolds. *Biomaterials* 25:1077–1086
78. Offeddu GS, Ashworth JC, Cameron RE, Oyen ML (2015) Multi-scale mechanical response of freeze-dried collagen scaffolds for tissue engineering applications. *J Mech Behav Biomed Mater* 42:19–25. <https://doi.org/10.1016/j.jmbbm.2014.10.015>
79. Oh YJ, Sekot G, Duman M, Chtcheglova L, Messner P, Peterlik H, Schäffer C, Hinterdorfer P (2013) Characterizing the s-layer structure and anti-s-layer antibody recognition on intact tannerella forsythia cells by scanning probe microscopy and small angle x-ray scattering. *J Mol Recognit* 26:542–549. <https://doi.org/10.1002/jmr.2298>
80. Oliver WC, Pharr GM (2004) Measurement of hardness and elastic modulus by instrumented indentation: advances in understanding and refinements to methodology. *J Mater Res* 19(1):3–20
81. Oropesa-Nuñez R, Keshavan S, Dante S, Diaspro A, Mannini B, Capitini C, Cecchi C, Stefani M, Chiti F, Canale C (2018) Toxic hypf-n oligomers selectively bind the plasma membrane to impair cell adhesion capability. *Biophys J* 114:1357–1367. <https://doi.org/10.1016/j.bpj.2018.02.003>
82. Oyen M (2011) Nanoindentation of biological and biomimetic materials. *Exp Tech* 37(1):73–87. <https://doi.org/10.1111/j.1747-1567.2011.00716.x>
83. Palomba R, Palange AL, Rizzuti IF, Ferreira M, Cervadoro A, Barbato MG, Canale C, Decuzzi P (2018) Modulating phagocytic cell sequestration by tailoring nanoconstruct softness. *ACS Nano* 12:1433–1444. <https://doi.org/10.1021/acsnano.7b07797>
84. Palombo F, Madami M, Stone N, Fioretto D (2014a) Mechanical mapping with chemical specificity by confocal Brillouin and Raman microscopy. *Analyst* 139:729–733. <https://doi.org/10.1039/c3an02168h>
85. Palombo F, Winlove CP, Edginton RS, Green E, Stone N, Caponi S, Madami M, Fioretto D (2014b) Biomechanics of fibrous proteins of the extracellular matrix studied by Brillouin scattering. *J R Soc Interface* 11:20140739. <https://doi.org/10.1098/rsif.2014.0739>
86. Pastorino L, Dellacasa E, Scaglione S, Giulianelli M, Sbrana F, Vassalli M, Ruggiero C (2014) Oriented collagen nanocoatings for tissue engineering. *Colloids Surf B: Biointerfaces* 114:372–378
87. Pawelec KM, Husmann A, Best SM, Cameron RE (2014) Understanding anisotropy and architecture in ice-templated biopolymer scaffolds. *Mater Sci Eng C Mater Biol Appl* 37:141–147. <https://doi.org/10.1016/j.msec.2014.01.009>
88. Peticaroli S, Nickels JD, Ehlers G, Sokolov AP (2014) Rigidity, secondary structure, and the universality of the boson peak in proteins. *Biophys J* 106(12):2667–2674
89. Pukhlyakova E, Aman AJ, Elsayad K, Technau U (2018) β -Catenin-dependent mechanotransduction dates back to the common ancestor of Cnidaria and Bilateria. *Proc Natl Acad Sci U S A* 115:6231–6236. <https://doi.org/10.1073/pnas.1713682115>
90. Qi C, Yan X, Huang C, Melerzanov A, Du Y (2015) Biomaterials as carrier, barrier and reactor for cell-based regenerative medicine. *Protein Cell* 6:638–653. <https://doi.org/10.1007/s13238-015-0179-8>
91. Randall JT, Vaughan JM (1979) Brillouin scattering in systems of biological significance. *Philos Trans R Soc Lond A* 293(1402):341–348
92. Rezende CA, Lee LT, Galembeck F (2009) Surface mechanical properties of thin polymer films investigated by AFM in pulsed force mode. *Langmuir* 25:9938–9946. <https://doi.org/10.1021/la9010949>
93. Rigato A, Miyagi A, Scheuring S, Rico F (2017) High-frequency microrheology reveals cytoskeleton dynamics in living cells. *Nat Phys* 13:771–775. <https://doi.org/10.1038/nphys4104>

94. Sadati M, Nourhani A, Fredberg JJ, Taheri Qazvini N (2014) Glass-like dynamics in the cell and in cellular collectives. *Wiley Interdiscip Rev Syst Biol Med* 6:137–149. <https://doi.org/10.1002/wsbm.1258>
95. Salem AK, Stevens R, Pearson RG, Davies MC, Tendler SJB, Roberts CJ, Williams PM, Shakesheff KM (2002) Interactions of 3T3 fibroblasts and endothelial cells with defined pore features. *J Biomed Mater Res* 61:212–217. <https://doi.org/10.1002/jbm.10195>
96. Sassi P, Caponi S, Ricci M, Morresi A, Oldenhof H, Wolkers WF, Fioretto D (2015) Infrared versus light scattering techniques to monitor the gel to liquid crystal phase transition in lipid membranes. *J Raman Spectrosc* 46:644–651. <https://doi.org/10.1002/jrs.4702>. <http://adsabs.harvard.edu/abs/2015JRSp...46..644S>
97. Sbrana F, Fotia C, Bracalello A, Baldini N, Marletta G, Ciapetti G, Boichicchio B, Vassalli M (2012) Multiscale characterization of a chimeric biomimetic polypeptide for stem cell culture. *Bioinspir Biomim* 7(4):046007
98. Scarcelli G, Yun SH (2007) Confocal Brillouin microscopy for three-dimensional mechanical imaging. *Nat Photonics* 2:39–43. <https://doi.org/10.1038/nphoton.2007.250>
99. Scarcelli G, Yun SH (2011) Multistage viba etalons for high-extinction parallel Brillouin spectroscopy. *Opt Express* 19(10):913–10922. <https://doi.org/10.1364/OE.19.010913>
100. Scarcelli G, Yun SH (2012) In vivo Brillouin optical microscopy of the human eye. *Opt Express* 20:9197–9202. <https://doi.org/10.1364/OE.20.009197>
101. Scarcelli G, Kim P, Yun SH (2011) In vivo measurement of age-related stiffening in the crystalline lens by Brillouin optical microscopy. *Biophys J* 101:1539–1545. <https://doi.org/10.1016/j.bpj.2011.08.008>
102. Scarcelli G, Polacheck WJ, Nia HT, Patel K, Grodzinsky AJ, Kamm RD, Yun SH (2015) Noncontact three-dimensional mapping of intracellular hydromechanical properties by Brillouin microscopy. *Nat Methods* 12:1132–1134. <https://doi.org/10.1038/nmeth.3616>
103. Scarponi F, Mattana S, Corezzi S, Caponi S, Comez L, Sassi P, Morresi A, Paolantoni M, Urbanelli L, Emiliani C et al (2017) High-performance versatile setup for simultaneous Brillouin-Raman microspectroscopy. *Phys Rev X* 7(3):031015
104. Schlüßler R, Möllmert S, Abuhattum S, Cojoc G, Müller P, Kim K, Möckel C, Zimmermann C, Czarnecki J, Guck J (2018) Mechanical mapping of spinal cord growth and repair in living Zebrafish larvae by Brillouin imaging. *Biophys J* 115(5):911–923
105. Schneider D, Gomopoulos N, Koh CY, Papadopoulos P, Kremer F, Thomas EL, Fytas G (2016) Nonlinear control of high-frequency phonons in spider silk. *Nat Mater* 15(10):1079
106. Schwarz US, Gardel ML (2012) United we stand – integrating the actin cytoskeleton and cell–matrix adhesions in cellular mechanotransduction. *J Cell Sci* 125:3051. <https://doi.org/10.1242/jcs.093716>. <http://jcs.biologists.org/content/early/2012/07/10/jcs.093716>
107. Scott ON, Begley MR, Komaragiri U, Mackin TJ (2004) Indentation of freestanding circular elastomer films using spherical indenters. *Acta Mater* 52:4877–4885. <https://doi.org/10.1016/j.actamat.2004.06.043>
108. Sebastian T, Schultheiss K, Obry B, Hillebrands B, Schultheiss H, Obry B (2015) Micro-focused Brillouin light scattering: imaging spin waves at the nanoscale. *Front Phys* 3:35. <https://doi.org/10.3389/fphy.2015.00035>. <http://adsabs.harvard.edu/abs/2015FrP.....3...35S>
109. Smith L, Ma P (2004) Nano-fibrous scaffolds for tissue engineering. *Colloids Surf B: Biointerfaces* 39(3):125–131
110. Smolyakov G, Pruvost S, Cardoso L, Alonso B, Belamie E, Duchet-Rumeau J (2016) AFM PeakForce QNM mode: evidencing nanometre-scale mechanical properties of chitin-silica hybrid nanocomposites. *Carbohydr Polym* 151:373–380. <https://doi.org/10.1016/j.carbpol.2016.05.042>
111. Sneddon IN (1965) The relation between load and penetration in the axisymmetric boussinesq problem for a punch of arbitrary profile. *Int J Eng Sci* 3(1):47–57. [https://doi.org/10.1016/0020-7225\(65\)90019-4](https://doi.org/10.1016/0020-7225(65)90019-4)
112. Solano I, Parisse P, Gramazio F, Ianeselli L, Medagli B, Cavalleri O, Casalis L, Canepa M (2017) Atomic force microscopy and spectroscopic ellipsometry combined analysis of small ubiquitin-like modifier adsorption on functional monolayers. *Appl Surf Sci* 421:722–727. <https://doi.org/10.1016/j.apsusc.2016.10.195>

113. Sweers K, van der Werf K, Bennink M, Subramaniam V (2011) Nanomechanical properties of α -synuclein amyloid fibrils: a comparative study by nanoindentation, harmonic force microscopy, and peakforce QNM. *Nanoscale Res Lett* 6(1):270. <https://doi.org/10.1186/1556-276x-6-270>
114. Tomar V, Qu T, Dubey DK, Verma D, Zhang Y (2015) Introduction. In: Multiscale characterization of biological systems. New York: Springer-Verlag <https://doi.org/10.1007/978-1-4939-3453-9>
115. Traverso AJ, Thompson JV, Steelman ZA, Meng Z, Scully MO, Yakovlev VV (2015) Dual Raman-Brillouin microscope for chemical and mechanical characterization and imaging. *Anal Chem* 87:7519–7523. <https://doi.org/10.1021/acs.analchem.5b02104>
116. Vacanti CA (2007) The history of tissue engineering. *J Cell Mol Med* 10(3):569–576. <https://doi.org/10.1111/j.1582-4934.2006.tb00421.x>. <https://onlinelibrary.wiley.com/doi/abs/10.1111/j.1582-4934.2006.tb00421.x>
117. Vacher R, Boyer L (1972) Brillouin scattering: a tool for the measurement of elastic and photoelastic constants. *Phys Rev B* 6(2):639
118. Vacher Sussner H, Schmidt M, Hunklinger S (1980) High resolution studies of Brillouin scattering in amorphous materials, Chap. 13. In: Maris HJ (ed) *Phonon scattering in condensed matter*. Springer, Boston, pp 61–64
119. Vacher R, Pelous J, Courtens E (1997) Mean free path of high-frequency acoustic excitations in glasses with application to vitreous silica. *Phys Rev B* 56(2):R481
120. Vassalli M, Sbrana F, Laurita A, Papi M, Bloise N, Visai L, Bochicchio B (2013) Biological and structural characterization of a naturally inspired material engineered from elastin as a candidate for tissue engineering applications. *Langmuir* 29(15):898–15906. <https://doi.org/10.1021/la403311x>
121. Vaughan J, Randall J (1980) Brillouin scattering, density and elastic properties of the lens and cornea of the eye. *Nature* 284(5755):489–491
122. Vezenov DV, Noy A, Rozsnyai LF, Lieber CM (1997) Force titrations and ionization state sensitive imaging of functional groups in aqueous solutions by chemical force microscopy. *J Am Chem Soc* 119(8):2006–2015
123. Vinckier A, Semenza G (1998) Measuring elasticity of biological materials by atomic force microscopy. *FEBS Lett* 430(1–2):12–16. [https://doi.org/10.1016/s0014-5793\(98\)00592-4](https://doi.org/10.1016/s0014-5793(98)00592-4)
124. Wake MC, Patrick CW, Mikos AG (1994) Pore morphology effects on the fibrovascular tissue growth in porous polymer substrates. *Cell Transplant* 3:339–343
125. Wang N, Tytell JD, Ingber DE (2009) Mechanotransduction at a distance: mechanically coupling the extracellular matrix with the nucleus. *Nat Rev Mol Cell Biol* 10(1):75
126. Welzel PB, Friedrichs J, Grimmer M, Vogler S, Freudenberg U, Werner C (2014) Cryogel micromechanics unraveled by atomic force microscopy-based nanoindentation. *Adv Health Mater* 3(11):1849–1853
127. Wen JH, Vincent LG, Fuhrmann A, Choi YS, Hribar KC, Taylor-Weiner H, Chen S, Engler AJ (2014) Interplay of matrix stiffness and protein tethering in stem cell differentiation. *Nat Mater* 13:979–987. <https://doi.org/10.1038/nmat4051>
128. Wolff L, Fernández P, Kroy K (2012) Resolving the stiffening-softening paradox in cell mechanics. *PLoS One* 7:e40063. <https://doi.org/10.1371/journal.pone.0040063>
129. Xavier JR, Thakur T, Desai P, Jaiswal MK, Sears N, Cosgriff-Hernandez E, Kaunas R, Gaharwar AK (2015) Bioactive nanoengineered hydrogels for bone tissue engineering: a growth-factor-free approach. *ACS Nano* 9(3):3109–3118
130. Xu J, Lauger K, Dransfeld K, Wilson I (1994) Thermal sensors for investigation of heat transfer in scanning probe microscopy. *Rev Sci Instrum* 65(7):2262–2266
131. Yun SH, Chernyak D (2018) Brillouin microscopy: assessing ocular tissue biomechanics. *Curr Opin Ophthalmol* 29:299–305. <https://doi.org/10.1097/ICU.0000000000000489>
132. Zeltinger J, Sherwood JK, Graham DA, Mueller R, Griffith LG (2001) Effect of pore size and void fraction on cellular adhesion, proliferation, and matrix deposition. *Tissue Eng* 7:557–572. <https://doi.org/10.1089/107632701753213183>
133. Zwanzig R, Mountain RD (1965) High-frequency elastic moduli of simple fluids. *J Chem Phys* 43(12):4464–4471